Analytical Damping Contribution Assessment Method of Multiconverters System Based on Energy Network Model

Letian Wang, Jing Ma, *Senior Member, IEEE*, Peng Cheng, *Member, IEEE*, Hongfei Shao, and Yaqi Shen

***Abstract*—Multiconverters connected to grid can induce subsynchronous oscillation (SSO). This article proposed an analytical damping contribution assessment method that can explicitly reveal how (positively or negatively) and to which degree each converter in the multiconverters system changes the system stability level. First, the energy network model of the multiconverters system that satisfies energy conservation is proposed. On this basis, a theory proof is presented that the real part of eigenvalue of SSO mode in the multiconverters system is equal to the sum of coefficient in the aperiodic components of the derivative of dynamic energies injected by each converter and dissipation energy of network, which illustrates analytically how the SSO stability level is shaped. The dynamic energy showing a decreasing trend is good for the oscillation to disappear, and the faster the dynamic energy decreases, the faster the oscillation amplitude decreases. Thus, how and to which degree converter changes stability level can be revealed by the changing trend and rate of its dynamic energy, respectively. Moreover, the expression of dynamic energy is brief, which is, thus, readily for online use, and is universal for converters with different control strategies. Finally, hardware in loop tests verifies that, eliminate converters' rapidly increasing dynamic energy, the unstable SSO converges rapidly, and eliminate converters' slowly increasing dynamic energy, the unstable SSO converges but slowly, and eliminate converters' decreasing dynamic energy, unstable SSO diverges more rapidly, which demonstrates that dynamic energy can precisely assess damping contribution of converter.**

***Index Terms*—Damping contribution assessment, energy network model, multiconverters system, subsynchronous oscillations (SSOs).**

I. Introduction

With the wide application of converters in power generation, transmission, and distribution, the traditional energy conversion equipment has been replaced by power electronic devices, and the dynamic characteristics of the power system have undergone tremendous changes [1]. The subsynchronous oscillation (SSO) that occurs frequently is one of the key bottlenecks restricting the stable operation of the multiconverters-based power system [2]–[5]. For restraining the oscillations from spreading and ensuring the stable operation of system, identifying the root cause for oscillation in time is essential. Therefore, it is imperative to study the damping contribution assessment method.

1) Currently, methods used to track damping contribution mainly include the following:
2) energy flow method;
3) subsynchronous power method;
4) subsynchronous impedance method;
5) improved participation factor analysis method.

The energy flow method is a classical online damping contribution assessment method proposed early [6]–[8], and it has been verified in the industry application [9]. This method establishes a quantitative relationship between the change trend of energy flow and oscillation amplitude. So, the damping contribution of equipment to system stability can be evaluated by the change trend of its corresponding energy flow. However, the aforementioned quantitative relationship is derived based on the phasor model [6]–[9], which is quite different from the concerned SSO that is generally perceived as electromagnetic transient scale problem. So, this method is hard to track the damping contribution to SSO. The subsynchronous power method and the subsynchronous impedance method proposed recently are available for the SSO problem [10]–[13], and their principles are similar. Based on the physical concept that negative resistor is not conducive to stability and produces negative power, converters with negative power output make negative damping effect on system, so realizing damping assessment. However, the equivalent negative resistor only indicates that there is a risk of instability [14]. To determine if the multiconverters system is unstable quantitatively, the Nyquist criterion or eigenvalue should be used as in [15]–[18]. Therefore, the aforementioned two methods are only suitable for identifying whether the converter is an oscillation source, but it is hard to explicitly quantify to which degree each converter in the multiconverters system changes the system stability level. The improved participation factor method is proposed recently that can get quantitative results rigorously [19]–[22]. Through sensitivity analysis, the quantitative relationship between the apparatus,

Manuscript received 31 December 2021; revised 15 March 2022 and 23 May 2022; accepted 30 May 2022. Date of publication 2 June 2022; date of current version 26 July 2022. This work is supported by National Natural Science Foundation of China under Grant 52130709. Recommended for publication by Associate Editor A. Davoudi. *(Corresponding author: Jing Ma.)*

The authors are with the State Key Laboratory of Alternate Electrical Power System with Renewable Energy Sources, North China Electric Power University, Beijing 102206, China (e-mail: hdwanglt@163.com; hdmajing@163.com; p.cheng@ncepu.edu.cn; 934358046@qq.com; jsntsyq1994@163.com).

Color versions of one or more figures in this article are available at https://doi.org/10.1109/TPEL.2022.3179694.

Digital Object Identifier 10.1109/TPEL.2022.3179694

states, or parameters and the stability level is studied, and the root cause for oscillation is obtained. But the sensitivity-based analysis requires high model integrity and parameter accuracy, and it is very difficult and inconvenient to obtain all equipment models and parameters of large-scale converters system, so the feasibility and accuracy of this method are greatly reduced. And, calculating the sensitivity of large-scale systems is very complex and time-consuming, which also limits the online use of this method.

To sum up, the abovementioned methods are either hard to be applied to electromagnetic transient scale oscillation analysis, or difficult to quantify to which degree a single equipment change the overall system stability level, or the stability analysis requires high model accuracy and complex calculation process. In view of the abovementioned problems, considering that all converters in the multiconverters system are connected to the network through specific ports, based on the dynamic energy on the corresponding converter connection port, this article reveals a brief and analytical relationship between port connection converter dynamics and the overall system stability level, so as to realize damping contribution assessment. Compared with traditional methods, this article has the following contributions.

1) This new energy-based stability analysis method is suitable for electromagnetic transient scale oscillation analysis. Compared with the traditional energy flow method [6]–[9], the application scope is further extended.
2) The analytical form of dynamic energies summed one by one as stability criteria is brief and clear to help know how the SSO stability level is shaped, so it is convenient to reveal analytically how and to which degree each converter in multiconverters system changes stability level.
3) The expression of dynamic energy is brief as the expression of traditional energy flow [9], which is, thus, readily for online use, and is universal for converters with different control strategies.

The remainder of this article is organized as follows. In Section II, the basic frame of the conventional energy flow method is reviewed. In Section III, an energy network model of the multiconverters system that satisfies energy conservation is constructed. And Section IV presents the analytical relationship between the increase/decrease of dynamic energy injected by each converter and the divergence/convergence of amplitude of oscillation in the multiconverters system. Accordingly, it demonstrates analytically that how and to which degree converter changes the overall system stability level can be assessed by the dynamic energy. In Section V, the correctness of the proposed method is verified by hardware in loop tests. Finally, Section VI concludes this article.

II. Review of Conventional Energy Flow Method

The basic frame of the conventional energy flow method used for oscillation analysis is reviewed in this section. And the limitation of the conventional method is discussed.

A. Theory Basis

In [6]–[7], the expression of energy flow injected by *i*th generator bus to *j*th bus is

$$W_{ij} = \int \Delta P_{ij} d\Delta\theta_i + \int \Delta Q_{ij} d\Delta V_i \tag{1}$$

where ΔP_{ij} and ΔQ_{ij} are the deviations in active power and reactive power from *i*th bus to *j*th bus, respectively, $\Delta\theta_i$ is the deviations in voltage angle of *i*th bus, $\Delta V_i = \ln(U_i)$—$\ln(U_{i,s})$, U_i is the voltage amplitude of *i*th bus, $U_{i,s}$ is the steady-state value of U_i.

If $W_{ij}<0$, the generator dissipates the energy and provides positive damping to system, and vice versa. This criterion is proved by (8) in [6] for the single-machine system and by (19) in [23] for the multimachine system.

B. Application

Combined with the wide area measurement system (WAMS), the W_{ij} can be measured in real time [9], [24]. The detailed steps can be found in [9] and [24], which are summarized as follows.

Step 1: The data, i.e., active power, voltage, angle, etc., are collected by the WAMS.
Step 2: The obtained data are then decomposed into a number of oscillation modes.
Step 3: The energy flow is calculated based on the results from step 2.
Step 4: According the sign of energy flow, the damping contribution of each generator is revealed.

On this basis, the online emergency control [25], design of damping controller for low-frequency oscillation [26], [27], etc., can be realized.

C. Limitations

It can be found from [6]–[9] that the derivations and proofs of energy function as (1) in the conventional energy flow method are based on the quasi-static phasor modeling approach of synchronous generator and power network. Thus, the variables used in (1) are dominated by the fundamental frequency component of the system (50 or 60 Hz) [28]. And the energy flow method is usually used to deal with electromechanical oscillation problem (i.e., low-frequency oscillation).

However, for the SSO concerned in this article, the dynamic of variables is dominated by that of frequency component of the electromagnetic oscillation in system (the frequency is not 50 or 60 Hz). If we apply these variables into (1) directly, it may cause unreasonable stability assessment results, which is further verified by experimental test in Appendix A. The reason behind is that (1) is with simplification during the quasi-static phasor modeling and cannot completely capture the electromagnetic phenomena [28]. So, the conventional energy flow method may not be directly suitable for the SSO study.

Since the SSO caused by converters needs to be valued with the rapid development of the power converter-based renewable energy system, a new method is necessary to be proposed. In the

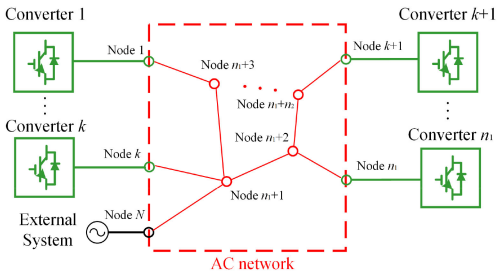

Fig. 1. Diagram of multiconverters system.

following sections, a new energy function is established based on the model of the converter system and without the assumption that electromagnetic transients are negligible, which is different from (1). Thus, compared with the conventional energy flow method, the proposed method can be applied to electromagnetic transient scale oscillation problem of the converters-based power system. The expression of energy functions of the proposed method is also brief as the expression of conventional energy flow, which is, thus, readily for online use. The proposed method is universal for converters with different control strategies.

III. Energy Network Model

A. Mathematical Model of Multiconverters System

Fig. 1 shows diagram of the multiconverters system. Suppose network in Fig. 1 contains N nodes and M branches. Among them, the N nodes ($N = n_1+n_2+1$) contained can be divided into the following three categories.

Category 1: The converter nodes defined as type A nodes, the total number of which is n_1, as the green circles in Fig. 1.
Category 2: The internal nodes of the network defined as type B nodes, the total number of which is n_2, as red circles in Fig. 1.
Category 3: The node connected to external grid defined as type C node, total number of which is 1, as black circle in Fig. 1.

The M branches ($M = m_1+m_2$) can be divided into the following two categories.

Category 1: The branches not directly connected with type C node defined as type A branch, the total number of which is m_1.
Category 2: The branches directly connected with type C node defined as type B branch, the total number of which is m_2.

1) Modeling of Power Network: According to the electrical network theory [28], the incidence matrix $\mathbf{A}_a$ of the network in Fig. 1 is

$$\mathbf{A}_a = \begin{array}{c} \\ \text{Node 1} \\ \text{Node 2} \\ \vdots \\ \text{Node } N \end{array} \begin{array}{c} \begin{array}{cccc} \text{Branch 1} & \cdots & \cdots & \text{Branch M} \end{array} \\ \begin{bmatrix} a_{11} & a_{12} & \cdots & a_{1M} \\ a_{21} & a_{22} & \cdots & a_{2M} \\ \vdots & \vdots & \ddots & \vdots \\ a_{N1} & a_{N2} & \cdots & a_{NM} \end{bmatrix} \end{array}. \tag{2}$$

In (2), if the mth branch is associated with the nth node and the branch direction deviates from the node, then the element $a_{nm} = 1$; if the mth branch is associated with the nth node and the branch direction points to the node, then the matrix element $a_{nm} = -1$, if mth branch is not related to nth node, $a_{nm} = 0$.

Furthermore, define the d-axis and q-axis components of voltage on the type C node as: u_{gd} and u_{gq}, which usually constant because the stiff large power grid. And define the type A and type B nodes voltage vectors in d-axis as $\boldsymbol{U}_{Sd}$ and $\boldsymbol{U}_{Nd}$, and in q-axis as $\boldsymbol{U}_{Sq}$ and $\boldsymbol{U}_{\mathrm{Nq}}$, respectively. The expressions of these voltage components are

$$\begin{cases} \boldsymbol{U}_{Sd} = \left[u_{Sd,1}\ u_{Sd,2}\ \cdots\ u_{Sd,n_1} \right] \\ \boldsymbol{U}_{Nd} = \left[u_{Nd,n_1+1}\ u_{Nd,n_1+2}\ \cdots\ u_{Nd,n_1+n_2} \right] \\ \boldsymbol{U}_{Sq} = \left[u_{Sq,1}\ u_{Sq,2}\ \cdots\ u_{Sq,n_1} \right] \\ \boldsymbol{U}_{Nq} = \left[u_{Nq,n_1+1}\ u_{Nq,n_1+2}\ \cdots\ u_{Nq,n_1+n_2} \right] \end{cases}. \tag{3}$$

The d-axis current vectors on the type A and type B branches are defined as $\boldsymbol{I}_{Ld}$ and $\boldsymbol{I}_{gd}$, respectively, and the q-axis current vectors are defined as $\boldsymbol{I}_{Lq}$ and $\boldsymbol{I}_{gq}$, respectively. The expressions of these current components are

$$\begin{cases} \boldsymbol{I}_{Ld} = \left[i_{Ld,1}\ i_{Ld,2}\ \cdots\ i_{Ld,m_1} \right] \\ \boldsymbol{I}_{gd} = \left[i_{gd,m_1+1}\ i_{gd,m_1+2}\ \cdots\ i_{gd,m_1+m_2} \right] \\ \boldsymbol{I}_{Lq} = \left[i_{Lq,1}\ i_{Lq,2}\ \cdots\ i_{Lq,m_1} \right] \\ \boldsymbol{I}_{gq} = \left[i_{gq,m_1+1}\ i_{gq,m_1+2}\ \cdots\ i_{gq,m_1+m_2} \right] \end{cases}. \tag{4}$$

By combining (2)–(4), the differential equations of the network in Fig. 1 can be obtained, as shown in the following.

a) Differential Equations of Nodes: The equations of n_1 type A nodes are

$$\begin{cases} C_{S,i} \frac{du_{Sd,i}}{dt} = \omega_0 C_{s,i} u_{Sq,i} - \mathbf{A}_a(i,:) \begin{bmatrix} \mathbf{I}_{Ld} \\ \mathbf{I}_{gd} \end{bmatrix} + i_{Sd,i} \\ i = 1, 2, \ldots n_1 \\ C_{S,i} \frac{du_{Sq,i}}{dt} = -\omega_0 C_{s,i} u_{Sd,i} - \mathbf{A}_a(i,:) \begin{bmatrix} \mathbf{I}_{Lq} \\ \mathbf{I}_{gq} \end{bmatrix} + i_{Sq,i} \\ i = 1, 2, \ldots n_1 \end{cases}. \tag{5}$$

The equations of n_2 type B nodes are

$$\begin{cases} C_{N,j} \frac{du_{Nd,j}}{dt} = \omega_0 C_{N,j} u_{Nq,j} - \mathbf{A}_a(j,:) \begin{bmatrix} \mathbf{I}_{Ld} \\ \mathbf{I}_{gd} \end{bmatrix} \\ j = n_1+1, n_1+2, \ldots n_1+n_2 \\ C_{N,j} \frac{du_{Nq,j}}{dt} = -\omega_0 C_{N,j} u_{Nd,j} - \mathbf{A}_a(j,:) \begin{bmatrix} \mathbf{I}_{Lq} \\ \mathbf{I}_{gq} \end{bmatrix} \\ j = n_1+1, n_1+2, \ldots n_1+n_2 \end{cases}. \tag{6}$$

In (5) and (6), $C_{S,i}$ and $C_{N,j}$ are the capacitances connected at type A and type B nodes, respectively; $i_{Sd,i}$ and $i_{Sq,i}$ are the d-axis and q-axis output current of the ith converter connected at type A nodes, respectively.

Since the voltage at the type C node is constant without dynamic process, the differential equation of the type C node does not exist.

b) Differential Equations of Branches: The equations of m_1 type A branches and m_2 type B branches are shown in (7)

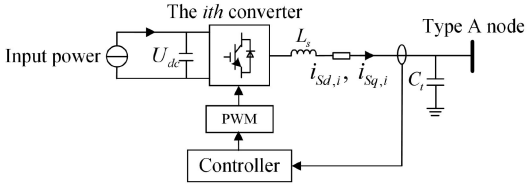

Fig. 2. Connection between *i*th converter and network.

and (8), respectively

$$\begin{cases} L_{n,l}\frac{di_{Ld,l}}{dt} = \omega_0 L_{n,l} i_{Lq,l} - R_l i_{Ld,l} + \mathbf{A}_a(:,l)^T \begin{bmatrix} \boldsymbol{U}_{Sd} \\ \boldsymbol{U}_{Nd} \end{bmatrix} \\ l = 1, 2, \ldots m_1 \\ L_{n,l}\frac{di_{Lq,l}}{dt} = -\omega_0 L_{n,l} i_{Ld,l} - R_l i_{Lq,l} + \mathbf{A}_a(:,l)^T \begin{bmatrix} \boldsymbol{U}_{Sd} \\ \boldsymbol{U}_{Nd} \end{bmatrix} \\ l = 1, 2, \ldots m_1 \end{cases} \tag{7}$$

$$\begin{cases} L_{g,z}\frac{di_{gd,z}}{dt} = \omega_0 L_{g,z} i_{gq,z} - R_z i_{gd,z} + \mathbf{A}_a(:,z)^T \begin{bmatrix} \boldsymbol{U}_{Sd} \\ \boldsymbol{U}_{Nd} \end{bmatrix} \\ -u_{gd} \quad z = m_1 + 1, \ldots m_1 + m_2 \\ L_{g,z}\frac{di_{gq,z}}{dt} = -\omega_0 L_{g,z} i_{Ld,l} - R_z i_{gq,z} + \mathbf{A}_a(:,z)^T \begin{bmatrix} \boldsymbol{U}_{Sd} \\ \boldsymbol{U}_{Nd} \end{bmatrix} \\ -u_{gq} \quad z = m_1 + 1, \ldots m_1 + m_2 \end{cases}. \tag{8}$$

In (7) and (8), $L_{n,l}$ and $L_{g,z}$ are the inductances connected in series with the type A and type B branches, respectively; R_l and R_z are the parasitic resistances of $L_{n,i}$ and $L_{g,z}$, respectively.

2) Modeling of Converters: The connection between the *i*th converter and network is shown in Fig. 2. No matter what control strategy the *i*th converter adopts, the linearized state-space model of the *i*th converter is given as

$$\begin{cases} \Delta\dot{\boldsymbol{x}}_i = A_i \Delta\boldsymbol{x}_i + B_i \Delta\boldsymbol{u_i} \\ \Delta\boldsymbol{y}_i = C_i \Delta\boldsymbol{x}_i + D_i \Delta\boldsymbol{u_i} \end{cases} \tag{9}$$

where Δ represents the small perturbation of a variable. A_i, B_i, C_i, and D_i are the state-space matrices, which is determined by $\boldsymbol{P}_i$ that is the set of filter and control parameter of the *i*th converter. $\Delta\boldsymbol{x}_i$ is the state variable vector of the *i*th converter. The input vector $\Delta\boldsymbol{u}_i = [\Delta u_{sd,i}, \Delta u_{sq,i}]$, i.e., type A node voltage in (5)**,** is the terminal voltage of the *i*th converter in *dq*-axis. The output vector $\Delta\boldsymbol{y}_i = [\Delta i_{Sd,i}, \Delta i_{Sq,i}]$ is the *d*-axis and *q*-axis output current of the *i*th converter connected at type A nodes.

By solving the linear differential equations, as shown in (9), $\Delta i_{Sd,i}$ and $\Delta i_{Sq,i}$ can be unified as the *implicit function* shown in (10), which is related to the filter and control parameters and terminal voltage of the *i*th converter

$$\begin{cases} \Delta i_{Sd,i} = h_{d,i}\left(\Delta\boldsymbol{u}_i, \boldsymbol{P}_i\right) \\ \Delta i_{Sq,i} = h_{q,i}\left(\Delta\boldsymbol{u}_i, \boldsymbol{P}_i\right) \end{cases}. \tag{10}$$

3) Modeling of Multiconverters System: The power network models (5)–(8) are linear. By substituting the *implicit function* (10) into (5), and combining with other network (6)–(8), the overall mathematical model of the multiconverters system can be obtained. According to (5)–(8), each differential equation in the obtained model can be written as the following general form:

$$c_{ii}\frac{d\Delta x_{ii}}{dt} = -b_{ii}\Delta x_{ii} + f_{ii} \tag{11}$$

where c_{ii} and b_{ii} are constant terms in *ii*th equation, Δx_{ii} represents the small perturbation of *ii*th state variables, and f_{ii} is the function composed of other state variables except Δx_{ii}.

And (11) helps us to clarify the general process of proposed energy network modeling method in following section.

B. Energy Network Model of Multiconverters System

Based on (11), the energy network model of the multiconverters system can be constructed by the following steps.

Step 1: Multiply both sides of (11) by the state variable in the differential symbol *d*()*/dt*, and then multiply the result by *dt*, which yields

$$c_{ii}\Delta x_{ii} d\Delta x_{ii} = -b_{ii}\Delta x_{ii}\Delta x_{ii} dt + f_{ii}\Delta x_{ii} dt. \tag{12}$$

Step 2: Integrate both sides of (12) with respect to *t*, so that the energy function corresponding to the *ii*th equation in mathematical model of the multiconverters system can be obtained

$$\frac{1}{2}c_{ii}\Delta x_{ii}^2 = -b_{ii}\int \Delta x_{ii}^2 dt + \int f_{ii}\Delta x_{ii} dt. \tag{13}$$

Step 3: Add up all the energy functions as the form of (13), so that the total energy function of the multiconverters system can be obtained

$$\frac{1}{2}\sum_{ii=1}^{N+M-1} c_{ii}\Delta x_{ii}^2 = -\sum_{ii=1}^{N+M-1} b_{ii}\int \Delta x_{ii}^2 dt + \sum_{ii=1}^{N+M-1} \int f_{ii}\Delta x_{ii} dt. \tag{14}$$

Step 4: According to [29] and [30], prove whether (14) satisfies the energy conservation condition or not. If it does, the construction of the energy network model is finished.

According to the abovementioned steps, follow steps 1 and 2 to obtain the detailed expressions of node and branch energy function as shown in (15)–(18).

1) The energy functions of n_1 type A nodes are

$$S_{Cs} = W_{Sc} + E_{\text{conv}} \tag{15}$$

where

$$\begin{cases} S_{Cs} = \sum_{i=1}^{n_1} S_{Cs,i} = \frac{1}{2}\sum_{i=1}^{n_1} C_{S,i}\Delta u_{Sd,i}^2 + C_{S,i}\Delta u_{Sq,i}^2 \\ W_{Sc} = \sum_{i=1}^{n_1} W_{Cs,i} \\ = \int \begin{pmatrix} -\sum_{i=1}^{n_1}\Delta u_{Sd,i}\left(\sum_{l=1}^{m_1} a_{il}\Delta i_{Ld,l}\right. \\ \left. +\sum_{z=m_1+1}^{m_1+m_2} a_{iz}\Delta i_{gd,z}\right) \\ -\sum_{i=1}^{n_1}\Delta u_{Sq,i}\left(\sum_{l=1}^{m_1} a_{il}\Delta i_{Lq,l}\right. \\ \left. +\sum_{z=m_1+1}^{m_1+m_2} a_{iz}\Delta i_{gq,z}\right) \end{pmatrix} dt \\ E_{\text{conv}} = \sum_{i=1}^{n_1} E_{\text{conv},i} \\ = \int \left(\sum_{i=1}^{n_1}\Delta u_{Sd,i}\Delta i_{Sd,i} + \Delta u_{Sq,i}\Delta i_{Sq,i}\right) dt \end{cases}.$$

In (15), $S_{Cs,i}$ is the stored energy of the ith type A node; $W_{Sc,i}$ is the interaction energy between the ith type A node and the branches it is connected with; $E_{\mathrm{conv},i}$ is the dynamic energy injected by the ith converter form its terminal port.

Because $i_{Sd,i}$ and $i_{Sq,i}$ in $E_{\mathrm{conv},i}$ is the implicit function of control parameters of ith converter according to (10), the expression of dynamic energy $E_{\mathrm{conv},i}$ is universal no matter what control strategy the converter adopts. And how $E_{\mathrm{conv},i}$ changes the system stability level is introduced latter in (28). Thus, the converter port dynamics on the system stability can be assessed.

2) The energy functions of n_2 type B nodes are

$$S_{Ns} = W_{Nc} \tag{16}$$

where

$$\begin{cases} S_{Ns} = \sum_{j=n_1+1}^{n_1+n_2} S_{Ns,j} \\ = \frac{1}{2}\sum_{j=n_1+1}^{n_1+n_2} C_{N,j}\Delta u_{Nd,j}^2 + C_{N,j}\Delta u_{Nq,j}^2 \\ W_{Nc} = \sum_{j=n_1+1}^{n_1+n_2} W_{Nc,j} \\ = \int \begin{pmatrix} -\sum_{j=n_1+1}^{n_1+n_2} \Delta u_{Nd,j} \left(\sum_{l=1}^{m_1} a_{jl}\Delta i_{Ld,l}\right. \\ \left. + \sum_{z=m_1+1}^{m_1+m_2} a_{jz}\Delta i_{gd,z}\right) - \\ \sum_{j=n_1+1}^{n_1+n_2} \Delta u_{Nq,j} \left(\sum_{l=1}^{m_1} a_{jl}\Delta i_{Lq,l}\right. \\ \left. + \sum_{z=m_1+1}^{m_1+m_2} a_{jz}\Delta i_{gq,z}\right) \end{pmatrix} dt \end{cases}.$$

In (16), $S_{Ns,j}$ is the stored energy of the jth type B node; $W_{Nc,j}$ is the interaction energy between the jth type B node and the branches it is connected with.

3) The energy functions of m_1 type A branches are

$$S_{Ln} = W_{n\mathrm{line}} + D_{Rn} \tag{17}$$

where

$$\begin{cases} S_{Ln} = \sum_{l=1}^{m_1} S_{Ln,l} = \frac{1}{2}\sum_{l=1}^{m_1} L_{n,l}\Delta i_{Ld,l}^2 + L_{n,l}\Delta i_{Lq,l}^2 \\ W_{n\mathrm{line}} = \sum_{l=1}^{m_1} W_{n\mathrm{line},l} \\ = \int \begin{pmatrix} \sum_{l=1}^{m_1} \Delta i_{Ld,l} \left(\sum_{i=1}^{n_1} a_{il}\Delta u_{Sd,i}\right. \\ \left. + \sum_{j=n_1+1}^{n_1+n_2} a_{jl}\Delta u_{Nd,j}\right) \\ + \sum_{l=1}^{m_1} \Delta i_{Lq,l} \left(\sum_{i=1}^{n_1} a_{il}\Delta u_{Sq,i}\right. \\ \left. + \sum_{j=n_1+1}^{n_1+n_2} a_{jl}\Delta u_{Nq,j}\right) \end{pmatrix} dt \\ D_{Rn} = \sum_{l=1}^{m_1} D_{Rn,l} = -\int \left(\sum_{l=1}^{m_1} R_l \left(\Delta i_{Ld,l}^2 + \Delta i_{Lq,l}^2\right)\right) dt \end{cases}.$$

In (17), $S_{Ln,l}$ is the stored energy of the lth type A branch; $W_{n\mathrm{line},l}$ is the interaction energy between the lth type A branch and the nodes it is connected with; $D_{Rn,l}$ is the dissipation energy generated by the resistance of the lth type A branch.

4) The energy functions of m_2 type B branches are

$$S_{Lg} = W_{g\mathrm{line}} + D_{Rg} + E_g \tag{18}$$

where

$$\begin{cases} S_{Lg} = \sum_{z=m_1+1}^{m_1+m_2} S_{Lg,z} = \frac{1}{2}\sum_{z=m_1+1}^{m_1+m_2} L_{g,z}\Delta i_{gd,z}^2 \\ \quad + L_{g,z}\Delta i_{gq,z}^2 \\ W_{g\mathrm{line}} = \sum_{z=m_1+1}^{m_1+m_2} W_{g\mathrm{line},z} \\ = \int \begin{pmatrix} \sum_{z=m_1+1}^{m_1+m_2} \Delta i_{gd,z} \left(\sum_{i=1}^{n_1} a_{iz}\Delta u_{Sd,i}\right. \\ \left. + \sum_{j=n_1}^{n_1+n_2} a_{jz}\Delta u_{Nd,j}\right) \\ + \sum_{z=m_1+1}^{m_1+m_2} \Delta i_{gq,z} \left(\sum_{i=1}^{n_1} a_{iz}\Delta u_{Sq,i}\right. \\ \left. + \sum_{j=n_1}^{n_1+n_2} a_{jz}\Delta u_{Nq,j}\right) \end{pmatrix} dt \\ D_{Rg} = \sum_{z=m_1+1}^{m_1+m_2} D_{Rg,z} \\ = -\int \left(\sum_{z=m_1+1}^{m_1+m_2} R_z \left(\Delta i_{gd,z}^2 + \Delta i_{gq,z}^2\right)\right) dt \\ E_g = \sum_{z=m_1+1}^{m_1+m_2} E_{g,z} \\ = -\int \left(\sum_{z=m_1+1}^{m_1+m_2} \left(\Delta i_{gd,z}\Delta u_{gd} + \Delta i_{gq,z}\Delta u_{gq}\right)\right) dt \end{cases}.$$

In (18), $S_{Lg,z}$ is the stored energy of the zth type B branch; $W_{g\mathrm{line},z}$ is the interaction energy between the zth type B branch and the nodes it is connected with; $D_{Rg,z}$ is the dissipation energy generated by the resistance of the zth type B branch; $E_{g,z}$ is the energy injected from external grid to the zth type B branch.

Follow Step 3, by adding up the energy functions of different types of nodes and branches shown in (15) to (18), the total energy function of the multiconverters system is obtained

$$\begin{aligned} &S_{Cs} + S_{Ns} + S_{Ln} + S_{Lg} \\ &\quad = E_{\mathrm{conv}} + E_g + (D_{Rn} + D_{Rg}) \\ &\qquad + (W_{Sc} + W_{Nc} + W_{n\mathrm{line}} + W_{g\mathrm{line}}). \end{aligned} \tag{19}$$

Since $W_{Sc}+W_{Nc}+W_{n\mathrm{line}}+W_{g\mathrm{line}} = 0$, (19) is equal to

$$\underbrace{S_{Cs} + S_{Ns} + S_{Ln} + S_{Lg}}_{S} = E_{\mathrm{conv}} + E_g + D_{Rn} + D_{Rg}. \tag{20}$$

And (20) is the expression of the energy network model. In order to verify whether (20) satisfies the energy conservation condition or not, define V as

$$V = (S_{Cs}+S_{Ns}+S_{Ln}+S_{Lg}) - (E_{\mathrm{conv}}+E_g+D_{Rn}+D_{Rg}). \tag{21}$$

Follow Step 4, the partial derivative of V in (21) with respect to time t is calculated [29] and [30]

$$\begin{aligned} \dot{V} = &\sum_{i=1}^{n_1} \left(\frac{\partial S_{Cs}}{\partial \Delta u_{Sd,i}} \cdot \frac{d\Delta u_{Sd,i}}{dt} + \frac{\partial S_{Cs}}{\partial \Delta u_{Sq,i}} \cdot \frac{d\Delta u_{Sq,i}}{dt}\right) \\ &+ \sum_{j=n_1+1}^{n_1+n_2} \left(\frac{\partial S_{Ns}}{\partial \Delta u_{Nd,j}} \cdot \frac{d\Delta u_{Nd,j}}{dt}\right. \\ &\left. + \frac{\partial S_{Ns}}{\partial \Delta u_{Nq,j}} \cdot \frac{d\Delta u_{Nq,j}}{dt}\right) \\ &+ \sum_{l=1}^{m_1} \left(\frac{\partial S_{Ln}}{\partial \Delta i_{Ld,l}} \cdot \frac{d\Delta i_{Ld,l}}{dt} + \frac{\partial S_{Ln}}{\partial \Delta i_{Lq,l}} \cdot \frac{d\Delta i_{Lq,l}}{dt}\right) \end{aligned}$$

$$+\sum_{z=m_1+1}^{m_1+m_2}\left(\frac{\partial S_{Lg}}{\partial \Delta i_{gd,z}}\cdot\frac{d\Delta i_{gd,z}}{dt}+\frac{\partial S_{Lg}}{\partial \Delta i_{gq,z}}\cdot\frac{d\Delta i_{gq,z}}{dt}\right)-\frac{d\left(E_{conv}+E_g+D_{Rn}+D_{Rg}\right)}{dt}=0. \tag{22}$$

In (22), it can be derived that the partial derivative of V with respect to t is 0, and the detailed process is shown in Appendix B. Thus, the energy network model in (20) satisfies the energy conservation condition [29] and [30], which is used for the analytical damping contribution assessment method design in next section.

IV. Analytical Damping Contribution Assessment Method of Multiconverters System

A. Theory Basis of the Proposed Method

In this section, the theory basis of the proposed method, i.e., the relationship between real part of eigenvalues and dynamic energies, is derived based on the energy network model in (20).

According to [28] and [29], when the multiconverters system is disturbed, causing SSO with mode $\alpha+j\omega_c$, the corresponding oscillation components in the voltages and currents of the system can be unified in the general form as

$$\Delta x_{ii}=A_{xi}e^{\alpha t}\cos(\omega_c t+\theta_{xi}) \tag{23}$$

where A_{xi} is amplitude of the oscillation component, θ_{xi} is phase of the oscillation components, α and ω_c are the real and imaginary part of eigenvalue of SSO mode, respectively.

In (23), if $\alpha<0$, the oscillation amplitude attenuates to 0, and the system is stable and vice versa. Hence, α reflects the stability level of SSO in the multiconverters system. And by deriving the analytical relation between α in (23) and the dynamic energy injected by each converter in (20), the analytical relationship between each converter and the stability level of SSO in multiconverters system can be derived.

First, according to [29] and [30], express the oscillation components in the voltage and current of system as the form of (23) and substitute them into (20). Then, calculate the derivatives of results with respect to t, where the periodic and aperiodic components are separated. Finally, the periodic components containing the product of exponential function and trigonometric function $K_{ac}e^{\alpha t}\cos(\omega_c t+\theta_{ac})$ are eliminated, and the aperiodic components containing the exponential function $K_{dc}e^{\alpha t}$ alone are preserved (K_{ac}, K_{dc} is constant item, and θ_{ac} is phase of trigonometric function).

According to the abovementioned steps, (24) can be derived.

$$\dot{S}_{dc}=\dot{E}_{conv\_dc}+\dot{D}_{Rn\_dc}+\dot{D}_{Rg\_dc} \tag{24}$$

where $\dot{S}_{dc}$, $\dot{E}_{conv\_dc}$, and $\dot{D}_{Rn\_dc}+\dot{D}_{Rg\_dc}$ are the aperiodic components of the derivatives of the stored energy, the dynamic energy, and the dissipation energy, respectively. And due to stiff external grid, the corresponding oscillation component in voltage is zero, causing aperiodic component of the derivative of E_g in (20) being zero, thus, does not exist in (24).

The above-mentioned aperiodic components reflect the change trend of the energy with time [29] and [30]. And (24) is expanded in detail shown in (25)–(27).

1) The aperiodic component of the derivative of the stored energy is

$$\dot{S}_{dc}=\alpha e^{2at}\begin{pmatrix}\sum_{i=1}^{n_1}\frac{C_{S,i}}{2}\left(\left(A_{uSd,i}^2+A_{uSq,i}^2\right)\right)\\+\sum_{j=n_1+1}^{n_1+n_2}\frac{C_{N,j}}{2}\left(\left(A_{uNd,j}^2+A_{uNq,j}^2\right)\right)\\+\sum_{l=1}^{m_1}\frac{L_{n,l}}{2}\left(\left(A_{iLd,l}^2+A_{iLq,l}^2\right)\right)\\+\sum_{z=m_1+1}^{m_1+m_2}\frac{L_{g,z}}{2}\left(\left(A_{igd,z}^2+A_{igq,z}^2\right)\right)\end{pmatrix}=\alpha e^{2at}\cdot w_s \tag{25}$$

where w_s is the coefficient in the aperiodic component of the derivative of the stored energy. $A_{iLd,l}$, $A_{iLq,l}$ and $A_{igd,z}$, $A_{igq,z}$ are the amplitudes of the oscillation components of d-axis and q-axis currents on the type A and B branches, respectively; $A_{uSd,i}$, $A_{uSq,i}$ and $A_{uNd,j}$, $A_{uNq,j}$ are the amplitudes of the oscillation components of d-axis and q-axis voltages at the type A and B nodes, respectively. Since w_s is always positive, if $\alpha>0$, the stored energy will increase with time and vice versa.

2) The aperiodic component of the derivative of the dynamic energy injected by converter is

$$\dot{E}_{conv\_dc}=e^{2at}\sum_{i=1}^{n_1}\frac{\begin{pmatrix}A_{uSd,i}A_{iSd,i}\cos(\theta_{uSd,i}-\theta_{iSd,i})\\+A_{uSq,i}A_{iSq,i}\cos(\theta_{uSq,i}-\theta_{iSq,i})\end{pmatrix}}{2}=e^{2at}\cdot\sum_{i=1}^{n_1}w_{E,i} \tag{26}$$

where $w_{E,i}$ is the coefficient in the aperiodic components of the derivative of the dynamic energy injected by the ith converter. $A_{iSd,i}$, $A_{iSq,i}$ and $\theta_{iSd,i}$, $\theta_{iSq,i}$ are the amplitudes and phases of the oscillation components of d-axis and q-axis currents injected by the ith converter, respectively. $\theta_{uSd,i}$ and $\theta_{uSq,i}$ are the phases of the oscillation components of d-axis and q-axis voltages at type A node, respectively.

The sign of $w_{E,i}$ indicates the change trend of dynamic energy, i.e., if $w_{E,i}>0$, the dynamic energy will increase with time. The absolute value of $w_{E,i}$ indicates the change rate of dynamic energy, i.e., the larger $w_{E,i}$, the faster the dynamic energy change.

3) The aperiodic component of the derivative of the dissipation energy is

$$\dot{D}_{Rn\_dc}+\dot{D}_{Rg\_dc}=-e^{2at}\sum_{l=1}^{m_1}\frac{R_l\left(A_{iLd,l}^2+A_{iLq,l}^2\right)}{2}$$

$$- e^{2at} \sum_{z=m_1+1}^{m_1+m_2} \frac{R_z \left(A_{igd,z}^2 + A_{igq,z}^2 \right)}{2}$$

$$= -e^{2at} \left(\sum_{l=1}^{m_1} w_{D,l} + \sum_{z=m_1+1}^{m_1+m_2} w_{D,z} \right) \quad (27)$$

where $w_{D,l}$ and $w_{D,z}$ are the coefficients in the aperiodic components of the derivatives of the dissipation energy of type A and type B branches. Since $w_{D,l}$ and $w_{D,z}$ are constantly positive, the dissipation energy keeps decreasing with time.

By applying (25)–(27) into (24), the analytical relationship between α in (23) and the aperiodic component of the derivative of the dynamic energy for ith converter $w_{E,i}$ can be obtained

$$\alpha = \frac{\sum_{i=1}^{n_1} w_{E,i}}{w_s} - \frac{\sum_{l=1}^{m_1} w_{D,l} + \sum_{z=m_1+1}^{m_1+m_2} w_{D,z}}{w_s} \quad (28)$$

where the real-part of SSO eigenvalue in multiconverters system α can be assessed by the sum of the coefficient in aperiodic components of the derivative of the dynamic energies injected by converters ($w_{E,i}$) and dissipation energy of network ($w_{D,l}$ and $w_{D,z}$).

And (28) reveals that the system damping [i.e., α in (28)] is shaped by the energy consumption [e.g., $-w_{D,l}/w_s < 0$, $-w_{D,z}/w_s < 0$, and $w_{E,i}/w_s < 0$ in (28)] or negative consumption [e.g., $w_{E,i}/w_s > 0$ in (28)] induced by different converters and network, which is the physic meaning behind (28) and analyzed as follows.

According to the Lyapunov's second principle [8], [27], [29], when the physic system is in a steady state, the operating point is $\boldsymbol{x} = \boldsymbol{x}_0$, and the corresponding stored energy is $S(\boldsymbol{x}_0)$. When the system is disturbed, the operating point is $\boldsymbol{x} = \boldsymbol{x}_0 + \Delta\boldsymbol{x}$, and the corresponding stored energy is $S(\boldsymbol{x}_0) + S(\Delta\boldsymbol{x})$. After the disturbance disappears, if $S(\Delta\boldsymbol{x})$ decreases to 0, $\Delta\boldsymbol{x}$ decreases to 0, and then $\boldsymbol{x}$ returns to the original state $\boldsymbol{x}_0$ (i.e., the system is stable). Conversely, if $S(\Delta\boldsymbol{x})$ increases, it causes $\Delta\boldsymbol{x}$ to increase, then $\boldsymbol{x}$ deviates from the original state $\boldsymbol{x}_0$ (i.e., the system is unstable). In sum, the more the stored energy in the physic system, the farther the system operating point $\boldsymbol{x}$ deviates from the equilibrium point $\boldsymbol{x}_0$, and vice versa.

The energy conservation condition as in (24) shows that the stored energy is equal to the sum of the dynamic energy and the dissipation energy. According to (24), when the dynamic energy injected by ith converter decreases over time [i.e., $w_{E,i}/w_s < 0$ in (28) where w_s is always positive], the stored energy is consumed (i.e., tends to decrease over time), which helps us to make $\boldsymbol{x}$ returns to $\boldsymbol{x}_0$, and vice versa. And due to $-w_{D,l}/w_s$ and $-w_{D,z}/w_s$ in (28) are always negative, the dissipation energy always decreases over time causing the stored energy to be consumed, which helps us to make $\boldsymbol{x}$ returns to $\boldsymbol{x}_0$. Therefore, it can be seen that the dynamic energies injected by different converters and dissipation energy induced by network produce damping effect. And they jointly shape the system damping, i.e., the real part of the eigenvalue α in (28).

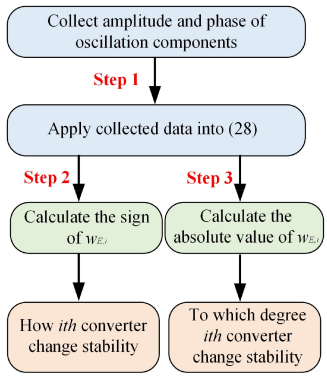

Fig. 3. Process of the application of the proposed method.

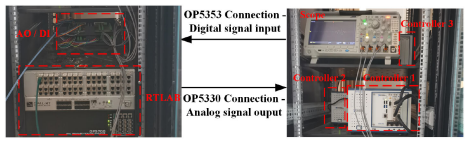

Fig. 4. HIL platform.

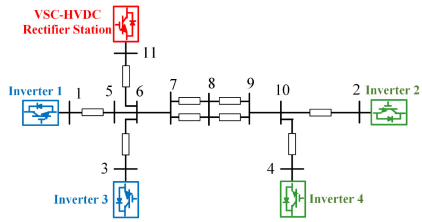

Fig. 5. Diagram of test system A.

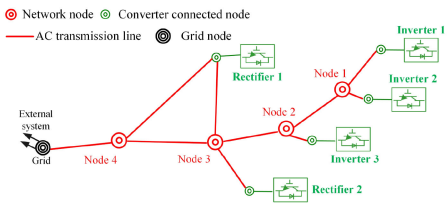

Fig. 6. Diagram of test system B.

B. Analytical Damping Contribution Assessment Method

Based on the form of the sum of $w_{E,i}$ in (28), an analytical damping contribution assessment method is proposed, where how (positively or negatively) and to which degree each converter in multiconverters system changes the system stability level can be explicitly revealed, as illustrated in Fig. 3. The major steps of the proposed method are summarized.

Step 1: Collect the amplitude and phase of the oscillation components in the voltage and current at each converter terminal port, and apply the collected data into (28).

Step 2: By calculating the sign of $w_{E,i}$, how each converter in the multiconverters system affects the stability can be revealed according to (28). If $w_{E,i} > 0$ (dynamic energy with increasing trend), converter i makes against for stability because it makes α increase. Conversely, if $w_{E,i} < 0$ (dynamic energy with

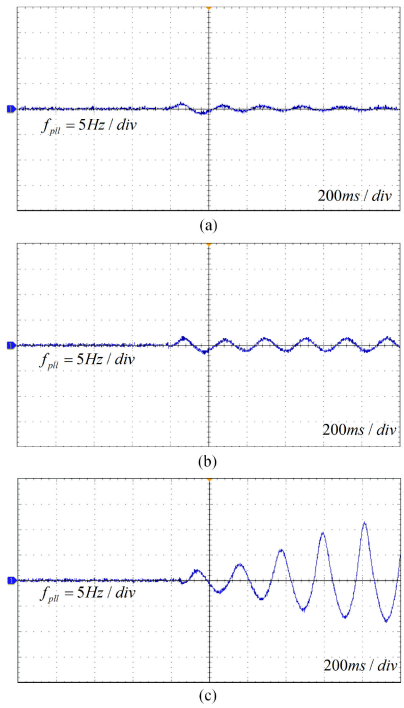

Fig. 7. HIL test results of three oscillation cases. (a) Converging oscillation. (b) Constant amplitude oscillation. (c) Diverging oscillation.

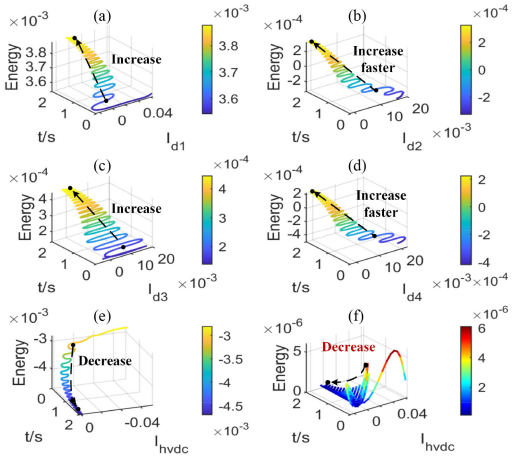

Fig. 8. Energy variation trajectory in the converging oscillation case. (a) $E_{\mathrm{conv},1}$. (b) $E_{\mathrm{conv},2}$. (c) $E_{\mathrm{conv},3}$. (d) $E_{\mathrm{conv},4}$. (e) $E_{\mathrm{conv},5}$. (f) $\sum_{i=1}^{5} E_{\mathrm{conv},i} + D_{Rn} + D_{Rg}$.

decreasing trend), converter i makes for stability because it makes α decrease.

Step 3: By calculating the absolute value of $w_{E,i}$, to which degree that ith converter changes stability level can be quantified according to (28). For example, for two different converter i and j, if $w_{E,i}>0$, $w_{E,j}>0$, and $w_{E,i}$ is larger than $w_{E,j}$ (dynamic energy of converter i has a faster change rate), the converter i deteriorates stability with a higher degree than converter j because it contributes much more to the increasing extent of α. And the differences of degree between converter

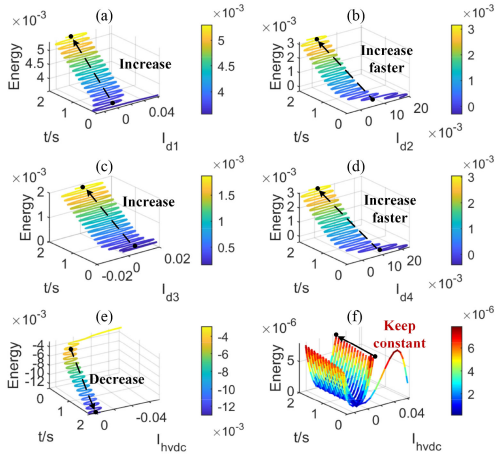

Fig. 9. Energy variation trajectory in the constant-amplitude oscillation case. (a) $E_{\mathrm{conv},1}$. (b) $E_{\mathrm{conv},2}$. (c) $E_{\mathrm{conv},3}$. (d) $E_{\mathrm{conv},4}$. (e)$E_{\mathrm{conv},5}$. (f) $\sum_{i=1}^{5} E_{\mathrm{conv},i} + D_{Rn} + D_{Rg}$.

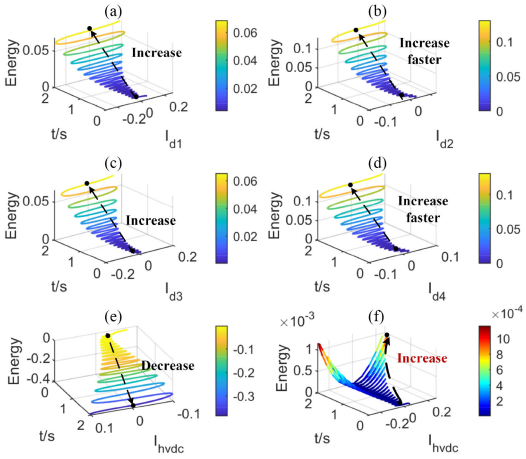

Fig. 10. Energy variation trajectory in the diverging oscillation case: (a) $E_{\mathrm{conv},1}$. (b) $E_{\mathrm{conv},2}$. (c) $E_{\mathrm{conv},3}$. (d) $E_{\mathrm{conv},4}$. (e) $E_{\mathrm{conv},5}$. (f) $\sum_{i=1}^{5} E_{\mathrm{conv},i} + D_{Rn} + D_{Rg}$.

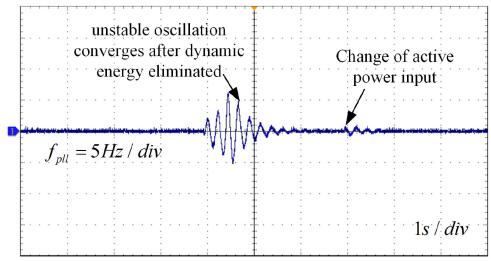

Fig. 11. HIL test result of scenario 1.

i and j deteriorate stability can be quantified as $\Delta w_{E,ij} = w_{E,i} - w_{E,j}$.

In addition, if all terms, i.e., $w_{E,i}$, $w_{D,l}$, $w_{D,z}$, and w_s in (28), are calculated, the whole system stability level α can be quantified. If α is negative but close to 0, it indicates that

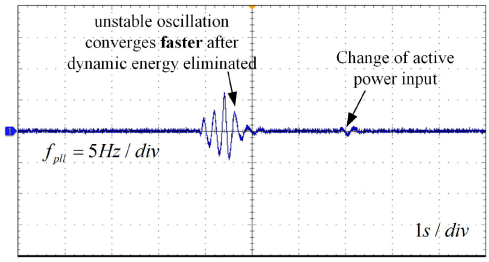

Fig. 12. HIL test result of scenario 2.

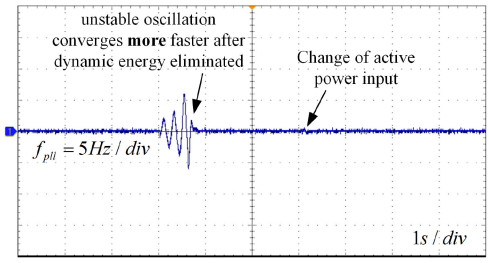

Fig. 13. HIL test result of scenario 3.

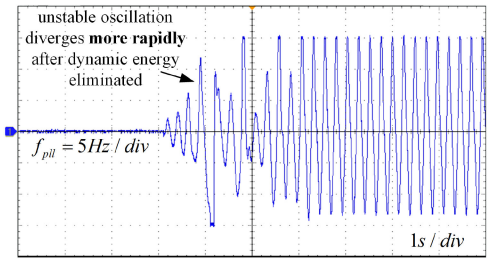

Fig. 14. HIL test result of scenario 4.

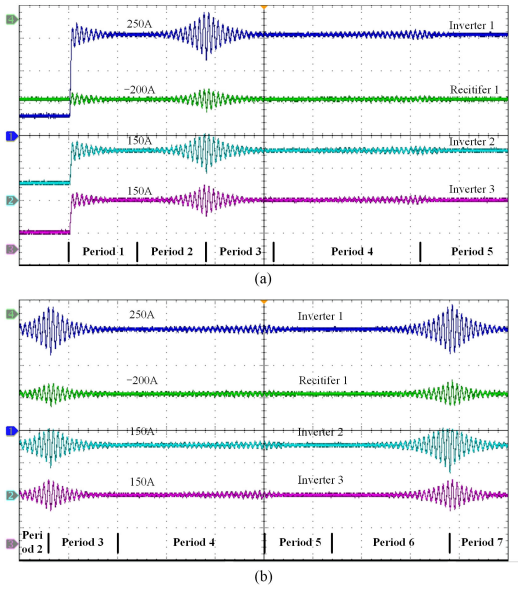

Fig. 15. Experimental waveform (0.5 s/div) of *d*-axis current of converters during the whole process of oscillation occurrence and development. (a) Waveform from period 1 to period 5. (b) Waveform from period 2 to period 7.

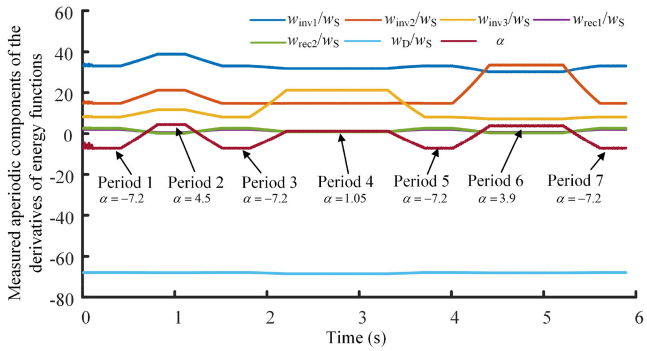

Fig. 16. Online measured results of (28) during the whole oscillation process (as shown in Fig. 15).

there is a limited stability margin. If α is negative but far from 0, it indicates a high stability margin. And if α is positive, it indicates instability. And the expression of $w_{E,i}$, $w_{D,l}$, $w_{D,z}$, and w_s is brief, which is, thus, readily for online use (see Section IV-C latter). It means that how the system stability level of SSO is shaped can be measured in real time. In the future, the abovementioned results can support to provide the system stability margin information and damping contribution information online for the wide-area SSO damping control in the multiconverters system, which helps us to promote system stability from the perspective of global stability.

C. Practical Considerations

The computation of $w_{E,i}$, $w_{D,l}$, $w_{D,z}$, and w_s is discussed in this section. It can be concluded from the following analysis that, for computation of $w_{E,i}$, $w_{D,l}$, $w_{D,z}$, and w_s, only the converter terminal voltage/current and fixed parameters of the resistances, inductances and capacitances in networks need to be considered. And the detailed explanations are shown as follows.

For the coefficient in aperiodic components of the derivatives of dynamic energy, i.e., $w_{E,i}$ in (26), it can be calculated just based on the terminal voltage and current of converter according to its expression. Thus, $w_{E,i}$ can be measured when the converter is black-box based.

For the coefficient in aperiodic components of the derivatives of stored energy and dissipation energy, i.e., w_s in (25) and $w_{D,l}$ and $w_{D,z}$ in (27), they need the: 1) voltage of the internal nodes of the network and current of the internal line of the network; 2) parameters of resistance, inductances, and capacitances in networks.

However, the networks parameters are often fixed and open for system operators, which is different from the converter that its manufacturers disclose their control algorithms to system operators. Thus, the calculations of stored energy and dissipation energy do not face the problem of black-box models. And if the terminal voltage of converter is obtained, the voltage and current of the internal nodes and line of the network can be calculated based on (6)–(8) indirectly. And the process is shown as follows.

Step 1: Equations (6)–(8) can form a linear state-space function.

In the function, the type A nodes voltage $\boldsymbol{U}_{Sd}$ and $\boldsymbol{U}_{Sq}$ (i.e.,

terminal voltage of converter) are input variable. And the voltage of the internal nodes of the network (i.e., type B nodes voltage $\boldsymbol{U}_{Nd}$ and $\boldsymbol{U}_{Nq}$) and the current of the internal line of the network (i.e., type A and type B branches current $\boldsymbol{I}_{Ld}$ and $\boldsymbol{I}_{Lq}$, $\boldsymbol{I}_{gd}$ and $\boldsymbol{I}_{gq}$) are output variable.

Step 2: On this basis, the voltage of the internal nodes of the network and current of the internal line of the network can be solved based on state-space function. And it should be pointed that, the state-space function is fixed (parameter of networks are often fixed) and linear, causing less computation burden.

Thus, the stored energy and dissipation energy can also be calculated just based on the terminal voltage of converter. In sum, it can conclude that the energy functions can only be calculated based on the terminal voltage/current of converter and fixed network parameters.

Moreover, the feasibility of collecting amplitude and phase of the oscillation components of terminal voltage/current of converter in Step 1 of Fig. 3 need to be considered. Although the amplitude and phase of the oscillation components are more easily captured when the system is critically stable ($\alpha = 0$), how to realize measurement when $\alpha \neq 0$ is a popular research topic recently and much progresses have been made [31]–[34]. These advanced signal analysis tools can be combined with the stability analysis method proposed in this article.

Based on the latest multimodal signal analysis tool, i.e., *multisynchrosqueezing transform* (MSST) [35], the number of SSO modes *N* along with the oscillatory frequencies *f*, corresponding magnitude *A*, phase angle θ, and damping factor α for each mode can be determined as in [34]. And for the approach in [34], the function iteration method in [35] is introduced to reduce substantially the calculation time of the algorithm and ensure that the approach has a good real-time performance. In addition, as shown in the results in [34, Fig. 3], MSST has the smallest Rényi entropy values under noisy conditions, and is expected to have a strong resistance to noise. Thus, the MSST-based SSO detection method is adopted. And it should be pointed that other advanced signal analysis tools can also be combined with the proposed theory in this article. And the processes of MSST-based algorithm are summarized as follow, and more detailed information can be found in [34].

Process 1: The collected signals of terminal voltage and current of converter are processed by MSST. And the instantaneous time-frequency representation of the signal is obtained.

Process 2: The mean-shift algorithm is applied to determine number of oscillation modes. The frequency of each mode is obtained using [34, eq. (13)].

Process 3: Each mode in the original signal can be reconstructed as [34, eq. (15)]. On this basis, the SSO modal parameters, including magnitude, phase angle, and damping factor, are obtained by [34, eq. (17)].

In this study, the update rate of data is 10 ms per cycle. And the algorithm is coded in MATLAB platform on a PC (with 16 GB RAM and 3.2GHz intel Core CPU) and generally takes less than 10 ms to obtain results.

D. Discussions on the Benefits of the Proposed Method

The benefits of the proposed method compared with other sensitivity-based small-signal stability analysis methods proposed recently [19]–[22] are discussed in this section.

1) *Benefit 1:* The approaches [19]–[21] still rely on known transfer functions or estimated poles and residues, which make it hard to analyze large-scale systems with only black-box models. Although the method in [22] fills this gap, it relies only on the magnitudes of frequency domain participation factor, which is hard to reveal how (positively or negatively) each converter changes system stability level.

Compared with the approaches [19]–[22], the energy function in this article can be calculated just based on the terminal voltage/current of converter, which needs not the analytical model of converter. Thus, it is convenient to be applied to the large-scale multiconverters system where converter is black-box based. And an analytical relationship between the real-part of eigenvalue of SSO mode and the aperiodic components of the derivative of dynamic energies injected by each converter is established as in (28). On this basis, it can explicitly reveal how (positively or negatively) and to which degree each converter in the multiconverters system changes the whole system stability level.

2) *Benefit 2:* The methods in [19]–[22] are based on the state-space matrix model or transfer function model, whose expressions rely on the steady-state operating point of system and converter parameters. Since the steady-state operating point and converter parameters can often vary over a large range as system condition changing, methods in [19]–[22] need to update the expressions of models iteratively to recheck stability analysis results. This process is complex and time-consuming especially when a large number of converters is considered, which is, thus, inconvenient for online application.

Compared with [19]–[22], the energy functions in the proposed method can be calculated without knowing the steady-state operating point and converter parameters. The reason is that the expressions of energy functions are the *implicit function* of the steady-state operating point and converter parameters, e.g., dynamic energy, i.e., $E_{\mathrm{conv},i}$ in (15), stored energy, i.e., $S_{Cs,i}$ in (15), $S_{Ns,j}$ in (16), $S_{Ln,l}$ in (17), and $S_{Lg,z}$ in (18), and dissipation energy, i.e., $D_{Rn,l}$ in (17) and $D_{Rg,z}$ in (18). Only the converter terminal voltage/current data collected from the existing oscillations in the system and the fixed networks parameters need to be considered for calculation. So, the iterative updating of expressions of energy functions is not required in the proposed stability analysis method. And online calculation is more convenient to realize. On this basis, the variation trajectory of system damping level and converter damping contribution can be monitored continuously based on the collected data from the existing oscillations in the system during the whole process of oscillation occurrence and development. And the monitoring results can further support the wide-area oscillation damping control conveniently.

V. Hardware-in-Loop (HIL) Tests

A. Test Platform

HIL tests are conducted to verify the effectiveness of the proposed method. The HIL platform consists of RTLAB, and three CPU controllers-based on PXI protocol, as shown in Fig. 4.

1) Description of Test System A: As shown in Fig. 5, a multiconverters system for test is built, where four inverters are integrated into the voltage-source converter-based high-voltage direct current transmission system (VSC-HVDC). In Fig. 5, the inverter 1 and 3 both apply the $V_{\rm dc}$-Q control strategy, as shown in Fig. 21 of Appendix C, the inverters 2 and 4 both apply the $V_{\rm dc}$-AVC control strategy shown in Fig. 22 of Appendix C, the rectifier of VSC-HVDC applies the *vf* control strategy, as shown in Fig. 23 of Appendix C. The control algorithms of inverter 1 to 4 operate in the CPU controller 1 to 2, and the primary circuit operate in RTLAB. The parameters used are listed in Appendix C-B.

2) Description of Test System B: As shown in Fig. 6, another multiconverter system for test is built, where three inverters simulate the generators (e.g., Type-4 wind or solar) and two rectifiers simulate the load, and they all connect to grid through inductive line. The circuit topology and controller diagram of converter are shown in Fig. 24 of Appendix C. And the parameters used are listed in Appendix C-C. The control algorithms of inverters and rectifiers operate in the CPU controller 1 to 3 that each CPU controller can generator two pulsewidth modulation waves to control two converters, and the primary circuit of power networks and converter operate in RTLAB.

B. Correctness Verification of Energy Network Model

The correctness verification of energy network model conducts on the test System A. First, tuning the parameters of ac voltage outer loop of inverter 2 and 4 as following 3 cases, where the basic parameters are shown in Appendix C-B.

1) Case 1: Tune k_{pac} and k_{iac} to -1.1 and -11, respectively.
2) Case 2: Tune k_{pac} and k_{iac} to -1.18 and -11.8, respectively.
3) Case 3: Tune k_{pac} and k_{iac} to -1.32 and -13.2, respectively.

Then, by making a step in active power input of inverter 1, three oscillation cases are excited, i.e., converging oscillation (Case 1), constant-amplitude oscillation (Case 2) and diverging oscillation (Case 3), as shown in Fig. 7. And the variation of phase lock loop (PLL) frequency $f_{\rm pll}$ of inverter 1 is recorded.

The oscillation components of voltage and current are extracted from the waveforms and applied to the expressions of $E_{{\rm conv},i}$, D_{Rn}, and D_{Rg}, so that the following can be calculated: 1) The trajectories changing with time of the dynamic energy injected by each inverters ($E_{{\rm conv},i}$, $i = 12,\ldots 4$) and rectifier in VSC-HVDC ($E_{{\rm conv},5}$); 2) The trajectory changing with time of the total energy $\sum_{i=1}^{5} E_{{\rm conv},i} + D_{Rn} + D_{Rg}$. The calculation results for cases 1–3 are shown in Figs. 8–10, respectively.

TABLE I
Change Trend of the Dynamic Energy Injected From Converters

Case	Inverter1	Inverter 2	Inverter 3	Inverter 4	HVdc
Case 1	↑	↑	↑	↑	↓
Case 2	↑	↑	↑	↑	↓
Case 3	↑	↑	↑	↑	↓

TABLE II
Change Rate of the Dynamic Energy Injected From Converters

Case	Inverter1	Inverter 2	Inverter 3	Inverter 4
Case 1	1.63×10^{-4}	$\mathbf{3.23\times10^{-4}}$	1.49×10^{-4}	$\mathbf{3.26\times10^{-4}}$
Case 2	8.68×10^{-4}	$\mathbf{16.1\times10^{-4}}$	8.53×10^{-4}	$\mathbf{17\times10^{-4}}$
Case 3	3.24×10^{-2}	$\mathbf{8.24\times10^{-2}}$	3.26×10^{-2}	$\mathbf{8.53\times10^{-2}}$

As can be seen from Figs. 8–10, the change trends of the total energy $\sum_{i=1}^{5} E_{{\rm conv},i} + D_{Rn} + D_{Rg}$ (increasing/decrease/keeping constant) are consistent with the time-domain results of diverging /converging/constant-amplitude oscillation, respectively, shown in Fig. 7. The abovementioned results demonstrate that the change trend of total energy can accurately determine if the system is stable, which verifies the correctness of the proposed energy network model in (20) and the analytical relationship between energy and real part of eigenvalue of SSO in (28).

C. Effectiveness Verification of the Analytical Damping Contribution Assessment Method

From experimental results in Figs. 8–10, the change trend and rate of dynamic energy injected by each inverter and rectifier in Fig. 5 are calculated, respectively. And the damping contribution assessment results are obtained, where the results of how (positively or negatively) each converter affects on stability are shown in Table I, and the results of to which degree each converter changes the stability level are shown in Table II.

From Table I, in three oscillation cases, the dynamic energy injected by inverters 1–4 all increase with time, and the dynamic energy injected by HVdc decreases with time. Hence, all inverters make against the stability, while the HVdc improves the stability. In addition, it can be seen from Table II that, the change rates of the dynamic energy injected by inverters applying different control strategies are obviously different. The change rates of the dynamic energy injected by inverters 2 and 4, which apply the $V_{\rm dc}$-AVC control strategy, are higher than those of inverters 1 and 3, which apply the $V_{\rm dc}$-Q control strategy. So, according to (28), inverters 2 and 4 deteriorate the stability level with a larger degree than inverters 1 and 3.

Based on the damping contribution assessment results mentioned above, we can make the following three predictions.

Prediction 1: Inverters 2 and 4 have a greater deterioration effect on the stability than inverters 1 and 3. Therefore, if the dynamic energies of inverters 2 and 4 are eliminated, the oscillation should converge faster compared with inverters 1 and 3 whose dynamic energies are eliminated.

Prediction 2: All inverters make against the stability. If the dynamic energies of all inverters are eliminated, the oscillation should converge faster than all scenarios in prediction 1.

Prediction 3: The rectifier of VSC-HVDC plays a role in improving the stability. Therefore, eliminating its dynamic energy, which wrongly removes the dynamic energy that is conducive to stability, should lead a further deterioration of damping.

Through experiment to verify whether the abovementioned predictions are correct, the effectiveness of the damping contribution assessment method can be verified. And a method that can eliminate dynamic energy by injecting additional subsynchronous oscillation current (ASOC) at the converter port (see Appendix D for detailed process [36]) is adopted in the experiment. And four scenarios in the following are set in experiment.

Scenario 1: The dynamic energies injected from inverters 1 and 3 are eliminated.

Scenario 2: The dynamic energies injected from inverters 2 and 4 are eliminated.

Scenario 3: The dynamic energies injected from all inverters are eliminated.

Scenario 4: The dynamic energy injected from the rectifier of VSC-HVDC is eliminated.

1) Test the prediction 1: The experimental results are shown in Figs. 11 and 12 (the parameters of Case 3 in Fig. 7 are used). From Figs. 11 and 12, the oscillation in scenario 2 disappears more rapidly compared with the results in scenario 1. And the step of active power input makes less obvious oscillations in scenario 2 compared with scenario 1. Those experimental results indicate a larger stability margin in scenario 2, which agree with prediction 1.

2) Test the prediction 2: The experimental result is shown in Fig. 13. Compared between Figs. 13 and 11–12, the attenuation speed of the oscillation in scenario 3 is significantly faster than that in scenario 1 and scenario 2. And the step of active power input hardly makes oscillations in scenario 3 compared with scenario 1 and scenario 2. Those experimental results indicate a higher stability level in scenario 3, which agree with the prediction 2.

3) Test the prediction 3: The experimental result is shown in Fig. 14. After the dynamic energy injected from the rectifier of VSC-HVDC being eliminated, the oscillation diverges more rapidly in scenario 4. The experimental result indicates deterioration of damping in scenario 4 compared with scenario 1 to 3, which agrees with the prediction 3.

In sum, the experiment results from Figs. 11–14 show that, eliminate the converters' rapidly increasing dynamic energy, the unstable oscillation converges rapidly, and eliminate the converters' dynamic energy with slow increasing trend, the unstable oscillation converges but slowly, and eliminate the converters' dynamic energy with decreasing trend, the unstable oscillation diverges more rapidly. These experiment results agree with the predictions and demonstrate the correctness of the damping contribution assessment results in Tables I and II. And it can conclude that the proposed method is able to accurately assess the damping contribution of each converter in the multiconverters system.

D. Comparison Verification Between the Proposed Method and Other Methods

1) Results of Experimental Waveform: The comparisons between the proposed method and other methods are conducted based on the following four cases in experiments (on the test System B). It not only aims to further verify the correctness of the proposed method but also verify the benefits (discussed in Section IV-D).

1) Case A: The base case, and the parameters used are listed in Appendix C-C.
2) Case B: The proportional gain of current loop PI controller of inverters 1–3 decrease to 0.7 times based on Case A.
3) Case C: the proportional gain of current loop PI controller of inverter 3 decreases to 0.45 times based on Case A.
4) Case D: The proportional gain of current loop PI controller of inverter 2 decreases to 0.45 times based on Case A.

The experimental waveform is presented in Fig. 15, which shows the whole process of oscillation occurrence and development under the switching among abovementioned four cases. The whole oscillation process in Fig. 15 can be divided into the following seven periods.

1) Period 1: Before the triggering of parameter changing, i.e., Case A, step the $I_{d\mathrm{ref}}$ of inverter 1, inverter 2, and inverter 3 to 200 A, 100 A, and 100 A, respectively. The system is with positive damping. This period lasted for 0.7 s.
2) Period 2: After the triggering of parameter changing, i.e., Case B, the system is instability, and the oscillation is amplified quickly. This period lasted for 0.7s.
3) Period 3: After the triggering of parameter changing, i.e., Case A, the system returns to positive damping. This period lasted for 0.7 s.
4) Period 4: After the triggering of parameter changing, i.e., Case C, the system is with weak negative damping and the oscillation is amplified slowly, which lasted for 1.5 s.
5) Period 5: After the triggering of parameter changing, i.e., Case A, the system returns to positive damping. This period lasted for 0.7 s.
6) Period 6: After the triggering of parameter changing, i.e., Case D, the system is instability, and the oscillation is amplified quickly. This period lasted for 1.2 s.
7) Period 7: After the triggering of parameter changing, i.e., Case A, the system returns to positive damping.

Fig. 16 provides the online measured results of (28) during the whole oscillation process (see Fig. 15). The w_{inv1}, w_{inv2}, w_{inv3}, w_{rec1}, and w_{rec2} are the measured coefficient in aperiodic components of the derivatives of dynamic energy for inverter 1, inverter 2, inverter 3, rectifier 1, and rectifier 2, respectively. w_{S} and w_{D} are the measured coefficient in aperiodic components of the derivatives of stored energy and dissipation energy, respectively. The measured real part of eigenvalue $\alpha = (w_{\mathrm{inv1}}+w_{\mathrm{inv2}}+ w_{\mathrm{inv3}}+ w_{\mathrm{rec1}}+ w_{\mathrm{rec2}}+ w_{\mathrm{D}})/ w_{\mathrm{S}}$, whose variation trajectory represents the system damping level during the whole oscillation process. The variation trajectory of $w_{\mathrm{inv1}}/w_{\mathrm{s}}$,

w_{inv2}/w_s, w_{inv3}/w_s, w_{rec1}/w_s, and w_{rec2}/w_s indicate the damping contribution of inverter 1, inverter 2, inverter 3, rectifier 1, and rectifier 2 during the whole oscillation process, respectively. For the results in Fig. 16, only the terminal voltage/current of converter and fixed networks parameters need to be considered for calculation.

2) Analysis of Measured System Damping Level: In Fig. 16, the measured α (after transient process) is less than 0 in Period 1, Period 3, Period 5, and Period 7, which indicates that the system is with positive damping. And the measured α is greater than 0 in Period 2 and Period 6, which indicates that the system is instability. And the measured α is greater than 0 in Period 4 but its value is close to 0, which indicates that the system is with weak negative damping. The abovementioned results obtained by the measured α agree with experimental waveforms (converges or being amplified) in the corresponding period of Fig. 15.

In sum, the comparison results demonstrate that, the proposed method can continuously and accurately monitor the variation trajectory of system damping level based on the collected data from the existing oscillations in the system during the whole process of oscillation occurrence and development.

3) Analysis of Measured Converter Damping Contribution: In all periods of Fig. 16, the measured value (after transient process) of w_{inv1}, w_{inv2}, and w_{inv3} are much larger than w_{rec1} and w_{rec2}. It indicates that the inverters have a greater negative damping contribution than rectifiers. This result agrees with the offline small-signal analysis result, i.e., interaction between PLL and current loop has a negative damping impact on SSO mainly in the inverter mode rather than rectifier mode (see [37, Fig. 7]).

In period 2, period 4, and period 6 of Fig. 16, it observes that w_{inv1}, w_{inv2}, and w_{inv3} vary as the corresponding inverter parameter changing (i.e., inverter 1, inverter 2 and inverter 3), which is illustrated as follows.

1) In period 2, after the triggering of parameter changing of all inverters, i.e., Case B, the measured value of w_{inv1}, w_{inv2}, and w_{inv3} all increase. And $w_{\mathrm{inv1}} > w_{\mathrm{inv2}} > w_{\mathrm{inv3}}$ in this period, where inverter 1 provides the maximum negative damping and inverter 3 provides the minimum negative damping.
2) In period 4, after the triggering of parameter changing of inverter 3, i.e., Case C, w_{inv3} increases mostly. And $w_{\mathrm{inv1}} > w_{\mathrm{inv3}} > w_{\mathrm{inv2}}$ in this period, where the negative damping contribution of inverter 3 exceeds inverter 2.
3) In period 6, after the triggering of parameter changing of inverter 2, i.e., Case D, w_{inv2} increases mostly. And $w_{\mathrm{inv2}} > w_{\mathrm{inv1}} > w_{\mathrm{inv3}}$ in this period, where the negative damping contribution of inverter 2 exceeds inverter 1.

The abovementioned observed results indicate that decreasing the proportional gain of current loop PI controller enlarges the negative damping contribution of inverter. This conclusion agrees with the offline small signal analysis results, i.e., the SSO can keep stable by increasing the proportional gain of the current controller (see [38, Fig. 10]).

And the aforementioned observed results in Fig. 16 also show that, relatively speaking, w_{inv1} is always the large one among w_{inv1}, w_{inv2} and w_{inv3}, and w_{inv3} is always the small one. From the location of inverter in Fig. 6, inverter 1 is the farthest from the grid, inverter 3 is the closest, and inverter 2 is in the center. The abovementioned results indicate that the farther the inverter is from the grid, the more negative damping contribution provided. This conclusion agrees with the offline small signal analysis results, i.e., long-distance transmission line leads to the deterioration of the dynamic characteristics of the PLL, resulting in the enhanced interaction with current loop and lower stability level (see [39, Fig. 8]).

TABLE III
DAMPING CONTRIBUTION ASSESSMENT RESULTS THROUGH METHOD IN [21]

Case	Inverter1	Inverter 2	Inverter 3	Rectifier 1	Rectifier 2
Period 2	**0.77**	0.49	0.16	0.05	0.03
Period 4	0.61	**0.28**	**0.39**	0.06	0.05
Period 6	**0.59**	**0.67**	0.15	0.08	0.06

Moreover, in order to further verify the correctness of the damping contribution results in Fig. 16, the sensitivity-based method [21] (layer 2) is applied to analyze system stability in period 2, period 4, and period 6. The results are shown in Table III, where the numerical values indicate the damping contribution of inverter 1, inverter 2, inverter 3, rectifier 1, and rectifier 2, respectively. It shows that the results obtained by [21] in the corresponding periods are consistent with the results in Fig. 16 of this article, e.g.,

i) in period 2, inverter 1 contributes the largest negative damping;
ii) in period 4, the negative damping contribution of inverter 3 enhances over inverter 2;
iii) in period 6, inverter 2 contributes the largest negative damping, where the negative damping contribution of inverter 1 is slightly smaller than inverter 2.

Based on those results, the correctness of the proposed method is further verified.

In sum, the abovementioned comparison results demonstrate that, the proposed method can continuously and accurately monitor the variation trajectory of damping contribution of each converter based on the collected data from the existing oscillations in the system during the whole process of oscillation occurrence and development.

4) Verification of Benefit of the Proposed Method: The methods in [21] are based on transfer function model, whose expressions rely on the steady-state operating point of system and converter parameters. Since the steady-state operating point and converter parameters can often vary over a large range during the whole process of oscillation occurrence and development as in Fig. 15, Zhu *et al.* [21] need to update transfer function model of converters system iteratively to recheck the stability results. And other small signal analysis methods [19]–[20], [22], [37]–[39] also need such iteration. Although the final result in Table III is the same as the result in Fig. 16 of this article, this iteration process is complex and time-consuming especially when a large number of converters is considered. So, the online use of those methods to continuously monitor the variation of damping contribution is inconvenient.

As for the proposed method, according to Fig. 16, the following can be found.

TABLE IV
COMPREHENSIVE COMPARISON WITH EXISTING METHODS

Method	EFM	SP/IM	IPFM			ENM
Ref.	[6-9]	[10-13]	[19-20]	[21]	[22]	This article
Req 1.	×	√	√	√	√	√
Req 2.	×	√	×	√	×	√
Req 3.	×	×	√	√	√	√
Req 4.	×	√	×	×	√	√
Req 5.	×	×	×	×	×	√

EFM: Energy flow method. **SP/IM**: Subsynchronous power method and the subsynchronous impedance method. **IPFM**: Improved participation factor method. **ENM:** Energy network model based analytical damping contribution assessment method. **Ref:** Reference**.**

1) The iterative updating of expressions of energy functions is not required in the stability analysis. Even if the operating point or converter parameter varies over large range during the whole process of oscillation occurrence and development as shown in Fig. 15, the proposed method can continuously monitor the variation trajectory of damping contribution of each converter based on the collected data from the existing oscillations in the system.
2) In addition, only the converter terminal voltage/current data collected from the existing oscillations in the system and the fixed networks parameters need to be considered for calculation in Fig. 16. And it does not have to know the analytical models of converters (black-box model is feasible).

E. Summary

In sum, based on the theoretical analysis in second paragraph of Section I, Section II-C, Section IV-D and experimental verifications in Section V-B, Section V-C, Section V-D, and Appendix A, the comprehensive comparisons between the proposed method and existing methods [6]–[13], [19]–[22] are conducted. The following five requirements (i.e., Req1 to Req 5), which are used to evaluate the performance of the damping contribution assessment method, are adopted for comparison.

Req 1: Suitable for the study of SSO.
Req 2: Suitable to reveal how (positively or negatively) each converter in multiconverters system changes the stability level of SSO.
Req 3: Suitable to reveal to which degree each converter in multiconverters system changes the stability level of SSO.
Req 4: Suitable for a large number of converters with black box model being considered.
Req 5: Suitable to continuously monitor the variation trajectory of damping contribution of each converter to SSO in real time.

And the comparison results are summarized in Table IV, where the abbreviations used are explained and listed in the following Table.

Since the EFM cannot satisfy the premise (i.e., Req 1) according to Section II-C and Appendix A, the Req 2 to Req 5 are also unsatisfied in Table IV. As for SP/IM and IPFM, it can be seen that both of SP/IM and IPFM fail to satisfy the Req 2, Req 3, and Req 4 simultaneously. The detailed reason is illustrated through lines 23 to 30 of the second paragraph in Section I and analysis in Section IV-D. And due to Req 3 is not satisfied for SP/IM and transfer function model updating process is needed for IPFM (illustrating in Section IV-D and in Section V-D.4), both of them cannot satisfy Req 5.

In contrast, those problems can be solved by the proposed method (ENM) that all the requirements in Table IV are satisfied simultaneously. And the satisfactions of all the requirements have been verified through experiment one by one, which is summarized as follows.

1) The satisfaction of Req 1 is verified by experimental results in Figs. 8, 9, 10, 16, and Fig. 20.
2) The satisfactions of Req 2 and Req 3 are verified by experimental results in Tables I, II, and Fig. 16.
3) The satisfactions of Req 4 and Req 5 are verified by experimental results in Fig. 16.

Thus, compared with the existing methods [6]–[13], [19]–[22], the proposed method gives more comprehensive performance in assessing damping contribution of each converter to SSO in multiconverters system.

VI. CONCLUSION

An analytical damping contribution assessment method is proposed, and the following conclusions are reached.

1) An energy network model satisfying energy conservation is proposed. Different from the traditional energy function method, it is suitable for the study of SSO in multiconverters-based power system.
2) A theory proof is presented that that the real-part of eigenvalue of SSO mode in multiconverters system is equal to the sum of the coefficient in the aperiodic components of the derivative of dynamic energies injected by each converter and dissipation energy of network, which illustrates analytically that how the SSO stability level is shaped. So, how (positively or negatively) and to which degree each converter in multiconverters system changes the system stability level can be revealed. Moreover, the expression of dynamic energy is brief, which is, thus, readily for online use, and it is also universal for converters with different control strategies.
3) The theory proof and proposed method can support to provide the stability margin information online for the wide-area SSO damping control of the multiconverters system in the future, which helps us to promote the system stability level from the perspective of global stability.

APPENDIX A

The experimental studies are further used to verify the conclusions in Section II-C. In the experiment, a grid-tied converter as shown in Fig. 17 is used, where the resistances in filter and equivalent grid impedance set both zero. Thus, the converter is the only device in the whole system that can provide damping and determines the system stability. And the basic parameters used are shown in Table V.

Three SSO oscillation cases are excited, i.e., unstable oscillation (by tuning k_p to 0.59 p.u.), constant-amplitude oscillation

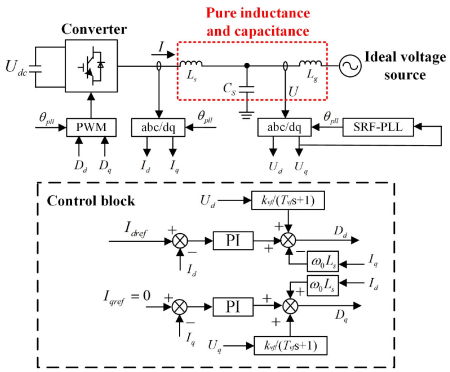

Fig. 17. Diagram of grid-tied converter.

TABLE V
PARAMETERS FOR GRID-SIDE CONVERTER

Symbol	Quantity	Value
S_b	Rated capacity	2MW
U_n	Rated line voltage	0.69kV
L_s	Inductance of filter	0.15 p.u.
C_t	Capacitance of filter	0.05 p.u.
L_g	Inductance in equivalent grid impedance	0.5 p.u.
k_p, k_i	PI parameters of current loop	0.8429 p.u., 19.3 p.u.
k_{p_pll}, k_{i_pll}	PI parameters of PLL	188.49 p.u., 3553 p.u.
T_{vf}	Time constant of voltage feedforward	0.01

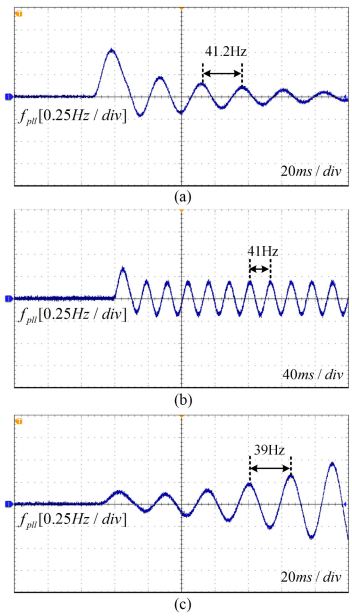

Fig. 18. Experimental waveform of f_{pll} under three oscillation cases. (a) Stable oscillation. (b) Constant-amplitude oscillation. (c) Unstable oscillation.

(by tuning k_p to 0.74 p.u.) and stable oscillation (by tuning k_p to 0.8 p.u.). The experimental waveforms of PLL frequency f_{pll} are shown in Fig. 18. And the oscillation frequencies in Fig. 18 are much higher than the frequency in traditional electromechanical oscillation [28].

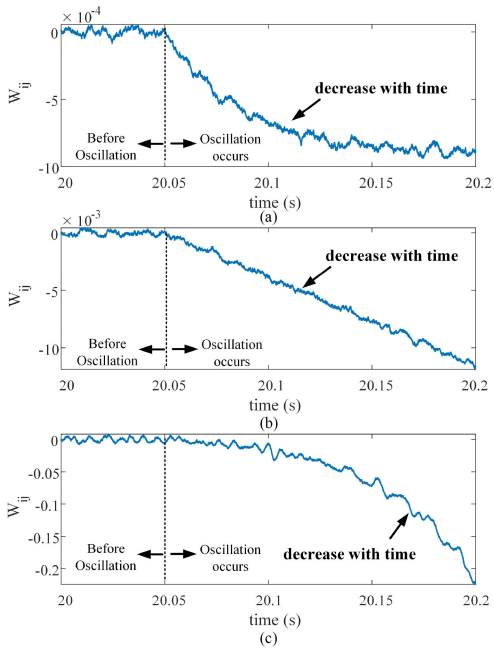

Fig. 19. Variation trajectory of conventional energy flow W_{ij} under three oscillation cases. (a) Stable oscillation. (b) Constant-amplitude oscillation. (c) Unstable oscillation.

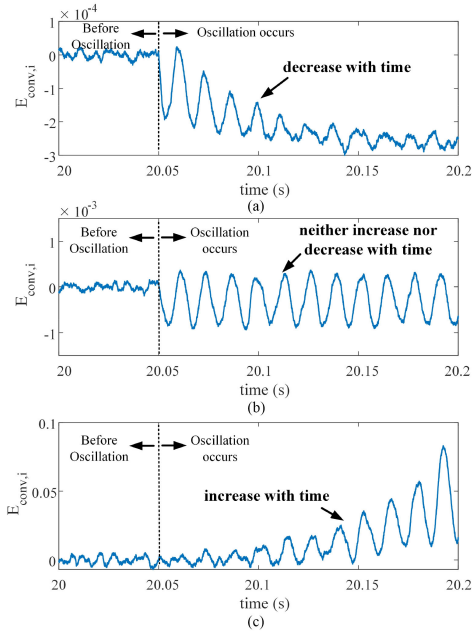

Fig. 20. Variation trajectory of proposed dynamic energy $E_{\mathrm{conv},i}$ under three oscillation cases. (a) Stable oscillation. (b) Constant-amplitude oscillation. (c) Unstable oscillation.

The measured data of waveforms under the abovementioned three cases are applied into (1) and (15), respectively. On this basis, the variation trajectory of energy flow W_{ij} and the dynamic energy $E_{\mathrm{conv},i}$ injected by converter in Fig. 17 are both calculated. And the results of the variation trajectory of energy flow W_{ij} and dynamic energy $E_{\mathrm{conv},i}$ are shown in Figs. 19 and 20, respectively.

From Fig. 19(a)–(c), it can be seen that the energy flow W_{ij} decreases with time (W_{ij} <0) under all three oscillation conditions. Even if the oscillation is unstable in Fig. 18(c), the corresponding damping contribution assessment result in Fig. 19(c) indicates that the converter produces positive damping contribution. On this basis, the system should be stable since only converter can provide damping in the whole system. However, such prediction of system stability is not consistent with the experimental waveform in Fig. 18(c). It means that the energy flow fails to assess the stability of SSO.

As for the dynamic energy proposed in this article, from Fig. 20(a), the dynamic energy $E_{\mathrm{conv},i}$ decreases with time [i.e., $w_{E,i}$<0 in (28)]. It indicates that converter produces positive damping contribution and the system should be stable. From Fig. 20(b), the dynamic energy $E_{\mathrm{conv},i}$ nearly neither increases nor decreases with time [i.e., $w_{E,i} = 0$ in (28)]. It indicates that converter produces nearly zero damping contribution and system should be at critical stable point. From Fig. 20(c), the dynamic energy $E_{\mathrm{conv},i}$ increases with time [i.e., $w_{E,i}$>0 in (28)]. It indicates that converter produces negative damping contribution and system should be unstable. The above predictions of system stability based on results in Fig. 20(a)–(c) agree with the experimental waveforms in Fig. 18(a)–(c), respectively. It means that the proposed dynamic energy can accurately assess the stability of SSO.

In sum, it can conclude that the conventional energy flow method may not be directly suitable for assessing the stability of SSO and the proposed dynamic energy can fill this gap. Since the SSO caused by converters needs to be valued with the rapid development of power converter based renewable energy system, the proposed method in this article is necessary.

APPENDIX B

The terms in (22) are expanded in detail and shown in (B-1)–(B-3). By applying (B-1)–(B-3) shown at the bottom of this page, into (22), it can be derived that the partial derivative of V with respect to t is 0

APPENDIX C

A. Control Block Diagram of Converters

This section presents the circuit and control block diagram of converters using different control algorism. The block diagram of converters using V_{dc}-Q mode shows in Fig. 21. The block

$$\begin{aligned}
&\sum_{i=1}^{n_1}\left(\frac{\partial S_{Cs}}{\partial u_{Sd,i}}\cdot\frac{du_{Sd,i}}{dt}+\frac{\partial S_{Cs}}{\partial u_{Sq,i}}\cdot\frac{du_{Sq,i}}{dt}\right)+\sum_{j=n_1+1}^{n_1+n_2}\left(\frac{\partial S_{Ns}}{\partial u_{Nd,j}}\cdot\frac{du_{Nd,j}}{dt}+\frac{\partial S_{Ns}}{\partial u_{Nq,j}}\cdot\frac{du_{Nq,j}}{dt}\right)\\
&=\sum_{i=1}^{n_1}\left(C_{S,i}u_{Sd,i}\frac{\sum_{i=1}^{n_1}i_{Sd,i}-\left(\sum_{l=1}^{m_1}a_{il}i_{Ld,l}+\sum_{z=m_1+1}^{m_1+m_2}a_{iz}i_{gd,z}\right)}{C_{S,i}}+C_{S,i}u_{Sq,i}\frac{\sum_{i=1}^{n_1}i_{Sq,i}-\left(\sum_{l=1}^{m_1}a_{il}i_{Ld,l}+\sum_{z=m_1+1}^{m_1+m_2}a_{iz}i_{gd,z}\right)}{C_{S,i}}\right)\\
&\quad+\sum_{j=n_1+1}^{n_1+n_2}\begin{pmatrix}C_{N,j}u_{Nd,j}\dfrac{-\left(\sum_{l=1}^{m_1}a_{jl}i_{Ld,l}+\sum_{z=m_1+1}^{m_1+m_2}a_{jz}i_{gd,z}\right)}{C_{N,j}}\\+C_{N,j}u_{Nq,j}\dfrac{-\left(\sum_{l=1}^{m_1}a_{jl}i_{Lq,l}+\sum_{z=m_1+1}^{m_1+m_2}a_{jz}i_{gq,z}\right)}{C_{N,j}}\end{pmatrix}
\end{aligned}\tag{B-1}$$

$$\begin{aligned}
&\sum_{l=1}^{m_1}\left(\frac{\partial S_{Ln}}{\partial i_{Ld,l}}\cdot\frac{di_{Ld,l}}{dt}+\frac{\partial S_{Ln}}{\partial i_{Lq,l}}\cdot\frac{di_{Lq,l}}{dt}\right)+\sum_{z=m_1+1}^{m_1+m_2}\left(\frac{\partial S_{Lg}}{\partial i_{gd,z}}\cdot\frac{di_{gd,z}}{dt}+\frac{\partial S_{Lg}}{\partial i_{gq,z}}\cdot\frac{di_{gq,z}}{dt}\right)\\
&=\sum_{l=1}^{m_1}\begin{pmatrix}L_{n,l}i_{Ld,l}\dfrac{\left(\left(\sum_{i=1}^{n_1}a_{il}u_{Sd,i}+\sum_{j=n_1+1}^{n_1+n_2}a_{jl}u_{Nd,j}\right)-R_l i_{Ld,l}\right)}{L_{n,l}}\\+L_{n,l}i_{Lq,l}\dfrac{\left(\left(\sum_{i=1}^{n_1}a_{il}u_{Sq,i}+\sum_{j=n_1+1}^{n_1+n_2}a_{jl}u_{Nq,j}\right)-R_l i_{Lq,l}\right)}{L_{n,l}}\end{pmatrix}\\
&\quad+\sum_{z=m_1+1}^{m_1+m_2}\begin{pmatrix}L_{g,z}i_{gd,z}\dfrac{\left(\left(\sum_{i=1}^{n_1}a_{iz}u_{Sd,i}+\sum_{j=n_1}^{n_1+n_2}a_{jz}u_{Nd,j}\right)-R_z i_{gd,z}-u_{gd}\right)}{L_{g,z}}\\+L_{g,z}i_{gq,z}\dfrac{\left(\left(\sum_{i=1}^{n_1}a_{iz}u_{Sq,i}+\sum_{j=n_1}^{n_1+n_2}a_{jz}u_{Nq,j}\right)-R_z i_{gq,z}-u_{gq}\right)}{L_{g,z}}\end{pmatrix}
\end{aligned}\tag{B-2}$$

$$\begin{aligned}
\frac{d\left(E_{conv}+E_g+D_{Rn}+D_{Rg}\right)}{dt}&=\left(\sum_{i=1}^{n_1}u_{Sd,i}i_{Sd,i}+u_{Sq,i}i_{Sq,i}\right)-\sum_{z=m_1+1}^{m_1+m_2}\left(i_{gd,z}u_{gd}+i_{gq,z}u_{gq}\right)\\
&\quad-\left(\sum_{l=1}^{m_1}R_l\left(i_{Ld,l}^2+i_{Lq,l}^2\right)+\sum_{z=m_1+1}^{m_1+m_2}R_z\left(i_{gd,z}^2+i_{gq,z}^2\right)\right).
\end{aligned}\tag{B-3}$$

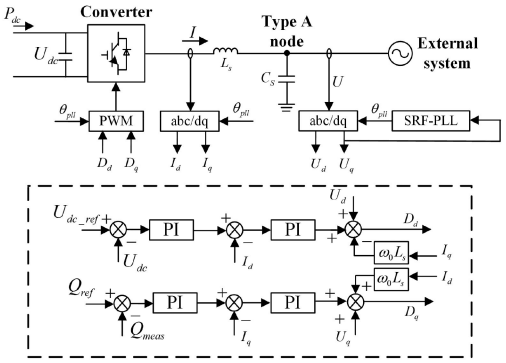

Fig. 21. Control block diagram of converters used $V_{\rm dc}$-Q mode.

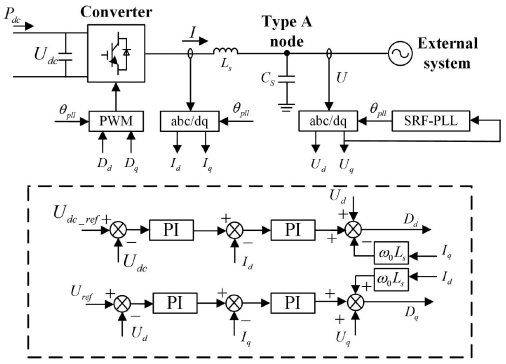

Fig. 22. Control block diagram of converters used $V_{\rm dc}$-AVC mode.

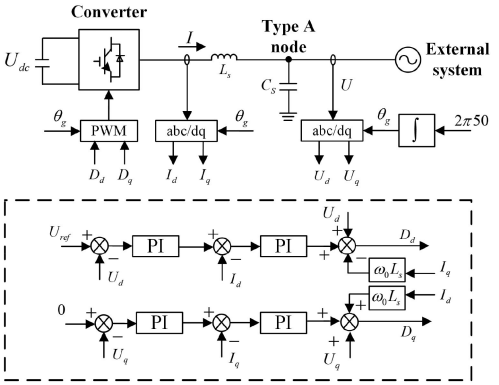

Fig. 23. Control block diagram of converters used *vf* mode.

diagram of converters using $V_{\rm dc}$-AVC mode shows in Fig. 22. The block diagram of converters using *vf* mode shows in Fig. 23. The block diagram of converters used in test system B shows in Fig. 24.

B. Parameter for Test System A

The basic parameters of $V_{\rm dc}$-Q control-based converter:

1) current inner loop: $k_{\rm pc} = 0.534$, $k_{\rm ic} = 53.46$;

2) DC voltage outer loop: $k_{\rm pp} = -1$, $k_{\rm ip} = -10$;

3) reactive power outer loop: $k_{\rm pq} = 0.001$, $k_{\rm iq} = 0.02$;

4) phase-locked loop: $k_{p\rm pll} = 0.67$, $k_{i\rm pll} = 38.2$;

5) filter inductance and capacitance: $L_s = 0.28$ mH, $C_s = 333$ μF.

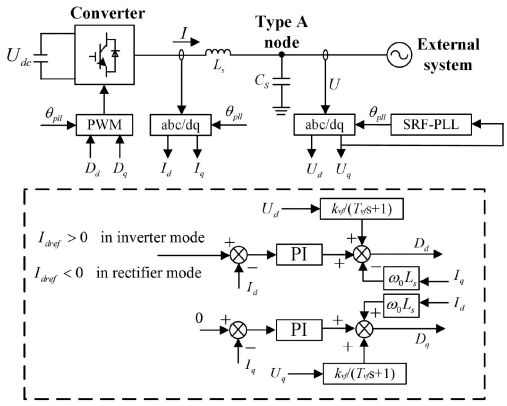

Fig. 24. Control block diagram of converters used in test system B.

The basic parameters of $V_{\rm dc}$-AVC control-based converter:

1) current inner loop: $k_{\rm pc} = 0.534$, $k_{ic} = 53.46$;

2) dc voltage outer loop: $k_{p\rm dc} = -1$, $k_{i\rm dc} = -10$;

3) ac voltage outer loop: $k_{p\rm ac} = -0.5$, $k_{i\rm ac} = -5$;

4) phase-locked loop: $k_{p\rm pll} = 0.67$, $k_{i\rm pll} = 38.2$;

5) filter inductance and capacitance: $L_s = 0.28$ mH, $C_s = 333$ μF.

The basic parameters of *vf* control-based converter:

1) Current inner loop: $k_{\rm pc} = 0.6$, $k_{ic} = 29.7$;

2) d-axis voltage outer loop: $k_{pd} = 3$, $k_{id} = 30$;

3) q-axis voltage outer loop: $k_{pq} = 3$, $k_{iq} = 30$;

4) Filter inductance and capacitance: $L_{\rm s} = 0.28$ mH, $C_{\rm s} = 333$ μF.

The parameters of lines

	$Z_{\rm line}$(1-5)	$Z_{\rm line}$(3-6)	$Z_{\rm line}$(2-10)	$Z_{\rm line}$(4-10)
R	20e-4Ω	40e-4Ω	40e-4Ω	20e-4Ω
L	0.1mH	0.08mH	0.05mH	0.07mH

The parameters of lines

	$Z_{\rm line}$(1-5)	$Z_{\rm line}$(3-6)	$Z_{\rm line}$(2-10)	$Z_{\rm line}$(4-10)
R	20e-4Ω	40e-4Ω	40e-4Ω	20e-4Ω
L	0.1mH	0.08mH	0.05mH	0.07mH

C. Parameter for Test System B

The basic parameters used for all converters are same as follows:

1) current inner loop: $k_{pc} = 0.297$, $k_{ic} = 40.5$;

2) voltage feedforward: $k_{vf} = 1$, $T_{vf} = 0.01$;

3) phase-locked loop: $k_{p\rm pll} = 0.167$, $k_{i\rm pll} = 9.55$;

4) filter inductance and capacitance: $L_{\rm s} = 0.28$ mH, $C_{\rm s} = 100$ μF.

The line between inverter 1 and node 1: 0.01 Ω+0.2 mH, the line between inverter 2 and node 1: 0.01 Ω+0.0015 mH, the line between inverter 3 and node 1: 0.01 Ω+0.05 mH, the line between rectifier 1 and node 3: 0.01 Ω+0.1 mH, the line between rectifier 1 and node 4: 0.01 Ω+0.1 mH, the line between rectifier 2 and node 3: 0 Ω+0.1 mH, the line between node 1 and node 2: 0.01 Ω+0.2 mH, the line between node 2 and node 3: 0.01 Ω+0.1 mH, the line between node 3 and node 4: 0.01 Ω+0.1 mH, the line between node 4 and grid:

0.01 Ω+0.125 mH, capacitance at node 1 is 1000 μF, capacitance at node 2 is 1000 μF, capacitance at node 3 is 2000 μF, capacitance at node 4 is 2000 μF.

APPENDIX D

In order to inject additional ASOC at the converter port, first, an additional power electronic device is connected in parallel at the converter port (the principle is similar to GTSDC that generates subsynchronous compensation current for synchronous generator as in [36]). And its control algorithms operate in the CPU controller 3 in Fig. 4. The amplitude and phase of the actual ASOC should meet: $A_{isd,h}{\approx}A_{isd}$, $A_{isq,h}{\approx}A_{isq}$ and $\theta_{isd,h}{\approx}\theta_{isd}{+}\pi$, $\theta_{isq,h}{\approx}\theta_{isq}{+}\pi$, where $A_{isd,h}$, $A_{isq,h}$ and $\theta_{isd,h}$, $\theta_{isq,h}$ are the amplitudes and phases of the ASOC in *dq*-axis, respectively, and A_{isd}, A_{isq} and θ_{isd}, θ_{isq} are the amplitudes and phases of the original ASOC of converter in *dq*-axis, respectively.

When an actual ASOC is generated by additional power electronic device, according to (26), the aperiodic component of the derivative of the additional dynamic energy generated by ASOC is

$$\Delta w_{E,i,} = \frac{\begin{pmatrix} A_{uSd,i}A_{iSd,ih}\cos(\theta_{uSd,i}-\theta_{iSd,ih}) \\ +A_{uSq,i}A_{iSq,ih}\cos(\theta_{uSq,i}-\theta_{iSq,ih}) \end{pmatrix}}{2}. \tag{D-1}$$

Because the amplitude of the ASOC is the same as that of subsynchronous current of converter, and the phase difference is 180°, the sum of (D-1) and $w_{E,i}$ of (26) is zero

$$\begin{aligned} w'_{E,i,} &= \Delta w_{E,i,} + w_{E,i,} \\ &= \frac{\begin{pmatrix} A_{uSd}A_{iSd,h}\cos(\theta_{uSd}-\theta_{iSd,h}) \\ +A_{uSq}A_{iSq,h}\cos(\theta_{uSq}-\theta_{iSq,h}) \end{pmatrix}}{2} \\ &+\frac{\begin{pmatrix} A_{uSd,i}A_{iSd,i}\cos(\theta_{uSd,i}-\theta_{iSd,i}) \\ +A_{uSq,i}A_{iSq,i}\cos(\theta_{uSq,i}-\theta_{iSq,i}) \end{pmatrix}}{2} = 0. \end{aligned} \tag{D-2}$$

From (D-2), it can be conclude that the dynamic energy injected into the system from the converter terminal port is eliminated.

REFERENCES

[1] X. Wang, F. Blaabjerg, and W. Wu, "Modeling and analysis of harmonic stability in an AC power-electronics-based power system," *IEEE Trans. Power Electron.*, vol. 29, no. 12, pp. 6421–6432, Dec. 2014.

[2] L. Fan and Z. Miao, "Wind in weak grids: 4 Hz or 30 Hz oscillations?," *IEEE Trans. Power Syst.*, vol. 33, no. 5, pp. 5803–5804, Sep. 2018.

[3] L. Huang *et al.*, "Grid-Synchronization stability analysis and loop shaping for PLL-based power converters with different reactive power control," *IEEE Trans. Smart Grid.*, vol. 11, no. 1, pp. 501–516, Jan. 2020.

[4] W. Du, X. Wang, and H. Wang, "Sub-synchronous interactions caused by the PLL in the grid-connected PMSG for the wind power generation," *Int. J. Electric Power Energy Syst.*, vol. 98, pp. 331–341, 2018.

[5] B. Wen, D. Boroyevich, R. Burgos, P. Mattavelli, and Z. Shen, "Analysis of D-Q small-signal impedance of grid-tied inverters," *IEEE Trans. Power Electron.*, vol. 31, no. 1, pp. 675–687, Jan. 2016.

[6] L. Chen, Y. Min, and W. Hu, "An energy-based method for location of power system oscillation source," *IEEE Trans. Power Syst.*, vol. 28, no. 2, pp. 828–836, May 2013.

[7] R. Xie and D. J. Trudnowski, "Tracking the damping contribution of a power system component under ambient conditions," *IEEE Trans. Power Syst.*, vol. 33, no. 1, pp. 1116–1117, Jan. 2018.

[8] Y. Yu, S. Grijalva, J. J. Thomas, L. Xiong, P. Ju, and Y. Min, "Oscillation energy analysis of inter-area low-frequency oscillations in power systems," *IEEE Trans. Power Syst.*, vol. 31, no. 2, pp. 1195–1203, Mar. 2016.

[9] S. Maslennikov and E. Litvinov, "ISO new england experience in locating the source of oscillations online," *IEEE Trans. Power Syst.*, vol. 36, no. 1, pp. 495–503, Jan. 2021.

[10] B. Gao, Y. Wang, W. Xu, and G. Yang, "Identifying and ranking sources of SSR based on the concept of subsynchronous power," *IEEE Trans. Power Del.*, vol. 35, no. 1, pp. 258–268, Feb. 2020.

[11] X. Xie, Y. Zhan, J. Shair, Z. Ka, and X. Chang, "Identifying the source of subsynchronous control interaction via wide-area monitoring of sub/super-synchronous power flows," *IEEE Trans. Power Del.*, vol. 35, no. 5, pp. 2177–2185, Oct. 2020.

[12] Y. Wang, X. Jiang, X. Xie, X. Yang, and X. Xiao, "Identifying sources of subsynchronous resonance using wide-area phasor measurements," *IEEE Trans. Power Del.*, vol. 36, no. 5, pp. 3242–3254, Oct. 2021.

[13] N. Yang *et al.*, "Defining SSO power and characterizing SSO propagation in power system with wind farms integration," *IEEE Trans. Power Syst.*, vol. 36, no. 4, pp. 3531–3540, Jul. 2021.

[14] G. Pinares and M. Bongiorno, "Modeling and analysis of VSC-Based HVDC systems for DC network stability studies," *IEEE Trans. Power Del.*, vol. 31, no. 2, pp. 848–856, Apr. 2016.

[15] M. K. Bakhshizadeh *et al.*, "Couplings in phase domain impedance modeling of grid-connected converters," *IEEE Trans. Power Electron.*, vol. 31, no. 10, pp. 6792–6796, Oct. 2016.

[16] A. Rygg, M. Molinas, C. Zhang, and X. Cai, "On the equivalence and impact on stability of impedance modeling of power electronic converters in different domains," *IEEE J. Emerg. Sel. Topics. Power Electron.*, vol. 5, no. 4, pp. 1444–1454, Dec. 2017.

[17] H. Zhang, L. Harnefors, X. Wang, H. Gong, and J. P. Hasler, "Stability analysis of grid-connected voltage-source converters using SISO modeling," *IEEE Trans. Power Electron.*, vol. 34, no. 8, pp. 8104–8117, Aug. 2019.

[18] J. Hu, Q. Hu, B. Wang, H. Tang, and Y. Chi, "Small signal instability of PLL-Synchronized type-4 wind turbines connected to high-impedance AC grid during LVRT," *IEEE Trans. Energy Convers.*, vol. 31, no. 4, pp. 1676–1687, Dec. 2016.

[19] E. Ebrahimzadeh, F. Blaabjerg, X. Wang, and C. L. Bak, "Bus participation factor analysis for harmonic instability in power electronics based power systems," *IEEE Trans. Power Electron.,* vol. 33, no. 12, pp. 10341–10351, Dec. 2018.

[20] Y. Zhan, X. Xie, H. Liu, H. Liu, and Y. Li, "Frequency-Domain modal analysis of the oscillatory stability of power systems with high-penetration renewables," *IEEE Trans. Sustain. Energy*, vol. 10, no. 3, pp. 1534–1543, Jul. 2019.

[21] Y. Zhu, Y. Gu, Y. Li, and T. C. Green, "Participation analysis in impedance models: The grey-box approach for power system stability," *IEEE Trans. Power Syst.*, vol. 37, no. 1, pp. 343–353, Jan. 2022.

[22] Y. Liao, X. Wang, and X. Wang, "Frequency-Domain participation analysis for electronic power systems," *IEEE Trans. Power Electron.*, vol. 37, no. 3, pp. 2531–2537, Mar. 2022.

[23] L. Chen, Y. Min, Y. P. Chen, and W. Hu, "Evaluation of generator damping using oscillation energy dissipation and the connection with modal analysis," *IEEE Trans. Power Syst.*, vol. 29, no. 3, pp. 1393–1402, May 2014.

[24] Y. Shu, X. Zhou, and W. Li, "Analysis of low frequency oscillation and source location in power systems," *CSEE J. Power Energy Syst.*, vol. 4, no. 1, pp. 58–66, Mar. 2018.

[25] L. Chen *et al.*, "Online emergency control to suppress frequency oscillations based on damping evaluation using dissipation energy flow," *Int. J. Electric Power Energy Syst.*, vol. 103, pp. 414–420, 2018.

[26] H. Li *et al.*, "Damping control strategies of inter-area low-frequency oscillation for DFIG-based wind farms integrated into a power system," *Int. J. Electric Power Energy Syst.*, vol. 61, pp. 279–287, 2014.

[27] C. Liu, G. Cai, W. Ge, D. Yang, C. Liu, and Z. Sun, "Oscillation analysis and wide-area damping control of DFIGs for renewable energy power systems using line modal potential energy," *IEEE Trans. Power Syst.*, vol. 33, no. 3, pp. 3460–3471, May 2018.

[28] P. Kundur, *Power System Stability and Control*. New York, NY, USA: McGraw-Hill, 1994.

[29] J. Ma, L. Wang, Y. Shen, and A. G. Phadke, "Interaction energy-based stability analysis method and application in grid-tied type-4 wind turbine generator," *IEEE J. Emerg. Sel. Topics. Power Electron.*, vol. 9, no. 5, pp. 5542–5557, Oct. 2021.

[30] J. Ma, L. Wang, and P. Cheng, "An active damping control strategy for grid-tied type-4 wind turbine generator based on energy feedback," *IEEE Trans. Power Electron.*, vol. 37, no. 5, pp. 5003–5020, May 2022.

[31] F. Zhang, L. Cheng, W. Gao, and R. Huang, "Synchrophasors-Based identification for subsynchronous oscillations in power systems," *IEEE Trans. Smart Grid.*, vol. 10, no. 2, pp. 2224–2233, Mar. 2019.
[32] X. Yang, J. Zhang, X. Xie, X. Xiao, B. Gao, and Y. Wang, "Interpolated DFT-Based identification of sub-synchronous oscillation parameters using synchrophasor data," *IEEE Trans. Smart Grid.*, vol. 11, no. 3, pp. 2662–2675, May 2020.
[33] L. Chen, W. Zhao, X. Xie, D. Zhao, and S. Huang, "Harmonic phasor estimation based on frequency-domain sampling theorem," *IEEE Trans. Instrum. Meas.*, vol. 70, 2021, Art. no. 9001210.
[34] Y. Ma, Q. Huang, Z. Zhang, and D. Cai, "Application of multisynchrosqueezing transform for subsynchronous oscillation detection using PMU data," *IEEE Trans. Ind. Appl.*, vol. 57, no. 3, pp. 2006–2013, May/Jun. 2021.
[35] G. Yu, Z. Wang, and P. Zhao, "Multisynchrosqueezing transform," *IEEE Trans. Ind. Electron.*, vol. 66, no. 7, pp. 5441–5455, Jul. 2019.
[36] X. Xie, L. Wang, and Y. Han, "Combined application of SEDC and GTSDC for SSR mitigation and its field tests," *IEEE Trans. Power Syst.*, vol. 31, no. 1, pp. 769–776, Jan. 2016.
[37] L. Harnefors, M. Bongiorno, and S. Lundberg, "Input-admittance calculation and shaping for controlled voltage-source converters," *IEEE Trans. Ind. Electron.*, vol. 54, no. 6, pp. 3323–3334, Dec. 2007.
[38] H. Gong, X. Wang, and L. Harnefors, "Rethinking current controller design for PLL-Synchronized VSCs in weak grids," *IEEE Trans. Power Electron.*, vol. 37, no. 2, pp. 1369–1381, Feb. 2022.
[39] X. Wang, M. G. Taul, H. Wu, Y. Liao, F. Blaabjerg, and L. Harnefors, "Grid-Synchronization stability of converter-based resources—An overview," *IEEE Open J. Ind. Appl.*, vol. 1, pp. 115–134, 2020.

Letian Wang was born in Ningxia Province, China. He received the B.S. degree from Wuhan University, Wuhan, China, in 2015.

He is currently a Doctoral Student with the School of Electrical and Electronic Engineering, North China Electric Power University, Beijing, China. His research interests include modeling and control of grid-connected converters, and stability analysis of power electronic-based power systems.

Jing Ma (Senior Member, IEEE) received the B.S. and Ph.D. degrees from North China Electric Power University, Beijing, China, in 2003 and 2008, respectively.

He has been a Visiting Research Scholar with the Bradley Department of Electrical and Computer Engineering, Virginia Polytechnic Institute and State University, Blacksburg, VA, USA, from 2008 to 2009. He is currently a Professor with the School of Electrical and Electronic Engineering, North China Electric Power University, China. His major interests include power system stability and control.

Peng Cheng (Member, IEEE) was born in Liaoning Province, China. He received the B.S. and Ph.D. degrees in electrical engineering from Zhejiang University, Hangzhou, China, in 2011 and 2016, respectively.

He is currently an Assistant Professor with the Department of China Institute of Energy and Transport Integration Development, North China Electric Power University. His current research interests include renewable energy-integrated transportation and multiconverter power systems.

Hongfei Shao was born in Shandong Province, China. He received the B.S. degree in 2020 from North China Electric Power University, Beijing, China, where he is currently working toward the master's degree with the School of Electrical and Electronic Engineering.

His research interests mainly include power system stability analysis and control.

Yaqi Shen was born in Jiangsu Province, China. She received the B.S. degree from North China Electric Power University, Beijing, in 2016. She is currently a Doctoral Student with the School of Electrical and Electronic Engineering, North China Electric Power University, Beijing, China. Her interests mainly include power system stability analysis and control.